The effect of crack length and maximum stress on the fatigue crack growth rates of engineering alloys

Amsterdam, E.; Wiegman, J. W. E.; Nawijn, M.; De Hosson, J. Th. M.

Published in:
International Journal of Fatigue

DOI:
10.1016/j.ijfatigue.2022.106919

Publication date:
2022

International Journal of Fatigue 161 (2022) 106919

Contents lists available at ScienceDirect

International Journal of Fatigue

journal homepage: www.elsevier.com/locate/ijfatigue

The effect of crack length and maximum stress on the fatigue crack growth rates of engineering alloys

E. Amsterdam [a,*], J.W.E. Wiegman [a], M. Nawijn [b], J.Th.M. De Hosson [c]

[a] Royal Netherlands Aerospace Centre (NLR), Marknesse, the Netherlands
[b] Colosso, Uffelte, the Netherlands
[c] Zernike Institute for Advanced Materials, University of Groningen, Groningen, the Netherlands

ARTICLE INFO

Keywords:
Total life approach
High cycle fatigue
Stress life
Short crack
Data analysis

ABSTRACT

The fatigue crack growth rate (FCGR) curve of metallic alloys is usually divided into three regions. Region II is often referred to as the Paris regime and is usually modelled with a power law relationship with a single exponent. Regions I and III are located at the beginning and end of the FCGR curve, respectively, and are frequently modelled with asymptotic relationships. In this paper we hypothesize that fatigue crack growth is governed by power law behaviour at all crack lengths and all stress intensity factor ranges (ΔK). To accommodate for the changes in the FCGR slope at regions I - III mathematical pivot points are introduced in the Paris equation. Power law behaviour with the presence of pivot points enables direct fitting of the crack length vs. cycles (*a-N*) curve to obtain the FCGR as a function of ΔK. This novel approach is applicable to small and long crack growth curves and results in accurate multilinear FCGR curves that are suitable for reconstruction of the measured *a-N* curves. The method is subsequently applied to *i*) different alloys to show local changes in the FCGR curve for changes in alloy composition and heat treatments, *ii*) naturally increasing ΔK testing of microstructurally small cracks to obtain accurate small crack FCGR data. The comparison with accurate long crack data shows that small cracks are faster, but the transition from region I to region II occurs at a specific fatigue crack growth rate which results in an apparent shift in ΔK at the transition. *iii*) Long cracks, which show that the FCGR increases with maximum stress for a given ΔK and stress ratio when the maximum stress approaches the yield stress. The maximum stress phenomenon becomes important in the case of fatigue testing, where the initial crack lengths are usually small and maximum stresses are high. It is concluded that for long cracks the phenomenon explains why the Paris equation is applicable rather at low maximum stress, while the Frost-Dugdale equation is more applicable at high maximum stress.

1. Introduction

The fatigue crack growth rate curve of metallic alloys is usually divided into three regions: region I corresponds to the steep slope in the fatigue crack growth rate (FCGR) curve near the threshold. Region II corresponds to a constant slope in the FCGR curve and region III is usually regarded as the steep slope prior to final failure of the specimen. For region II, Paris et al. empirically showed that the fatigue crack growth rate has a power law relationship with the stress intensity factor range, ΔK [1]:

$$\frac{da}{dN} = C(\Delta K)^n, \tag{1}$$

where da/dN is the fatigue crack growth rate and C and n are constants. The power law exponent, n, typically ranges between 2 and 5 for engineering alloys [2]. At the time of the introduction of Eq. (1), Paris and others also considered power law behaviour for region III and higher exponents were used to characterize the steeper slope in region III [3–6]. Similarly, Yokobori et al. found for mild steel that small cracks in region I also showed power law behaviour and the exponent for region I was 7.5, while the exponent for long cracks in region II was 2.5 [7,8]. Radhakrishnan fitted region I FCGR data of steel from various sources with Eq. (1) and concluded that the exponent in region I was about 4 times the exponent in region II (although in the paper regions I and II are called stage IIa and IIb, respectively) [9].

In fact, changes in the slope are not only limited to transitions

* Corresponding author.
E-mail address: emiel.amsterdam@nlr.nl (E. Amsterdam).

https://doi.org/10.1016/j.ijfatigue.2022.106919
Received 23 December 2021; Received in revised form 5 April 2022; Accepted 11 April 2022
Available online 13 April 2022

between regions I, II and III. In 1967, Wilhem showed that there is a knee, i.e. a change in exponent, in the region II fatigue crack growth rate curve when plotted on a double logarithmic scale [10]. The change in slope in region II was observed for multiple steel-, nickel-, titanium- and aluminium alloys [11–15]. Yoder et al. showed that the FCGR curves for 7XXX-series aluminium alloys (AA) exhibit a multilinear form when plotted double logarithmic over a sufficiently broad spectrum of ΔK (see Fig. 1) [16]. Wanhill showed for AA2024 that there are three transitions in the FCGR curve up to $\sim 10^{-7}$ m/cycle and Newman et al. used five linear segments to describe the FCGR curve of AA7075-T6 (see Fig. 1) [17,18]. Newman et al. used a look-up table to describe the FCGR curve, were the points in the table correspond to transition points between different slopes. The tabular data was obtained by visually drawing solid lines through the crack growth rate data [19]. They used this approach because a multilinear curve was able to describe the FCGR data more accurately than multi-parameter equations like the modified Paris or Forman equations [18]. The NASGRO and the Hartman-Schijve equation are examples of such equations and use asymptotic behaviour in regions I and III to fit FCGR data [20–22]. Modified Paris or Forman equations are frequently used to fit FCGR data that is obtained from the *a-N* curve using the secant and incremental polynomial method as described in ASTM E647 [23]. However, the secant and incremental polynomial methods do not result in noise free FCGR data. The amount of residual noise depends on the applied method applied, the error in the crack length measurement technique and the crack length measurement frequency [24,25].

Since the look-up table is able to describe the FCGR data more accurately than modified Paris or Forman equations [18], we introduced a pivot point to describe mathematically the change in the slope of the FCGR curve [26]:

$$\frac{da}{dN} = \frac{da}{dN_{TP}} \left(\frac{\Delta K}{\Delta K_{TP}} \right)^{n_i}, \tag{2}$$

where da/dN_{TP} and ΔK_{TP} are the FCGR and stress intensity factor range at the transition point (TP) where the exponent, n_i, is changing. Note that pivot points are used with regards to the transition points for changes in the slope of the FCGR curve. A pivot point basically corresponds to a point in the look-up table and was initially introduced to the Paris equation by McCartney et al. and Yokobori et al. based on dimensional analysis [27–29]. Radhakrishnan also used pivot points to correlate different exponents for different alloys, heat treatments and temperatures for a given region [9]. However, in these cases the pivot points were not used for a transition between two different slopes. Iost performed research on pivot points and the relationship between the constant, C, and the exponent, n in Eq. (1) [30,31]. Eventually, it was concluded that the pivot point is material-dependent and may be associated with a transition mechanism in the FCGR curve [32]. Amsterdam et al. were the first to introduce a pivot point to mathematically describe a change in the slope of the FCGR curve [26]. However, only one pivot point was used for a limited range of the FCGR curve.

In this paper we hypothesize that fatigue crack growth is governed by power law behaviour at all crack lengths and all ΔK values. To accommodate for changes in the slope of the FCGR curve, multiple pivot points are introduced in the FCGR equation, which results in a multilinear FCGR curve. The power law behaviour and the introduction of pivot points allow for direct fitting of the *a-N* curve to obtain the FCGR as a function of ΔK. Since this novel method generates the tabular data directly from the *a-N* curve and the data is suitable for an accurate reconstruction of the measured *a-N* curve, it eliminates the problem of fitting modified FCGR equations to noisy FCGR data obtained by the incremental polynomial method. FCGR tests on specimens from different alloy systems as well as tests on small and long crack specimens were performed to check the validity of method. The novel method is subsequently employed to observe changes in the FCGR data with alloy chemistry, heat treatment and the maximum stress used in a test.

2. Materials and methods

2.1. Materials

Test specimens were obtained from AA 7075-T7351 plate material with a thickness of 6.35 mm, AA 2524-T351 with a thickness of 8 mm and Inconel 601 with a thickness of 4 mm. A few specimens of 7075-T7351 were given an annealing heat treatment at 415 °C for 2 hr, furnace cool to 230 °C at 30 °C/hr, 6 hr at 230 °C and air cool (treatment f from Table 13 in [33]). A few specimens of 2524-T351 were given an annealing heat treatment at 415 °C for 2 hr, furnace cool to 260 °C at 30 °C/hr and air cool (treatment b from Table 13 in [33]).

2.2. Methods

2.2.1. Long crack specimen

Constant amplitude (CA) fatigue crack growth tests were performed on middle tension (M(T)) specimens at different maximum stress (S_{max}) and different stress ratio's ($R = S_{min}/S_{max}$). M(T) specimen with

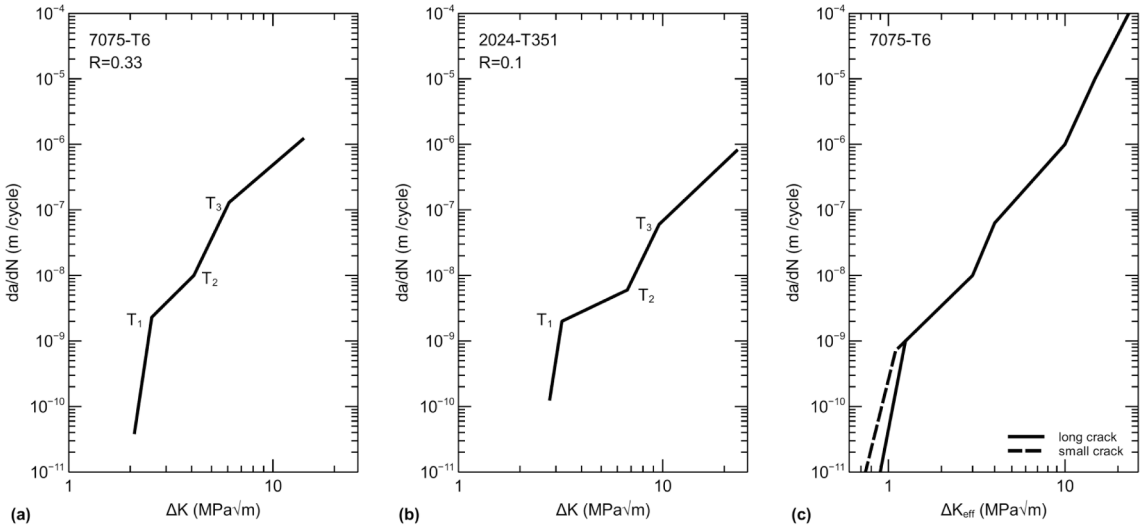

Fig. 1. Multilinear FCGR curves as a function of ΔK for (a) 7075-T6 and (b) 2024-T351. (c) Multilinear FCGR curve as a function of ΔK_{eff} for 7075-T6. Reproduced from [16], [17] and [18], respectively.

dimensions of 500 mm × 160 mm were removed from the plates of the given materials. The rolling direction was in the length of the specimens, hence loading-crack growth was in the L-T direction. Fatigue crack growth starter notches were central holes (1.6 mm diameter) with 0.7 mm deep electric discharge machined (EDM) slots on either side of the hole (total starter notch length of 3 mm). The EDM wire thickness was 0.16 mm. The area next to the starter notch was polished for optical crack growth measurements on both front and rear sides of the specimens. A constant amplitude 13.5 Hz sinusoidal load was introduced by a servo-hydraulic test machine with a 200 kN load cell. CA loading with the same maximum stress and stress ratio as for the actual test was used for pre-cracking the M(T) specimen to a single side crack length, a, of about 2 mm. The actual crack length after pre-cracking was measured with an optical travelling microscope.

Holes were drilled at 8 mm above and below the starter notch hole for copper pins. These were used for automated crack length measurements by direct current potential drop (DCPD). The current was introduced to the specimen at the specimen clamping. The potential drop of the specimen and a reference specimen was measured every 9 s by Matalect DCM-2 equipment using 12 readings and 11 samples. Potential drop data acquisition occurred every 100 or 200 cycles depending on the estimated number of cycles to failure. The DCPD data was converted to crack length data using Equation A2.5 in ASTM E647 [23]. V_r in Equation A2.5 in ASTM E647 was adjusted for each specimen such that the crack length from the DCPD measurement at the start of the test was equal to the crack length measured with the optical travelling microscope after pre-cracking. High resolution photographs of the front and rear side of the specimen with length markers were taken during initial tests to verify the DCPD measurements. The tests were performed in lab air environment.

The stress intensity factor range, ΔK, for the M(T) specimens is calculated by:

$$\Delta K = \beta(a)\Delta S\sqrt{\pi a}, \tag{3}$$

where ΔS is the stress range during the test and β the Feddersen final width correction that is calculated according to ASTM E647 [23]:

$$\beta = \sqrt{\sec\left(\frac{\pi a}{W}\right)}, \tag{4}$$

where W is the width of the specimen. The effective stress intensity factor range, ΔK_{eff}, is calculated using the Schijve crack closure correction [34,35]:

$$\Delta K_{eff} = \left(0.55 + 0.33R + 0.12R^2\right)\Delta K \tag{5}$$

2.2.2. Small crack specimens

Flat dogbone specimens were machined from the same 7075-T7351 plate as the M(T) specimens and tested with alternating CA and variable amplitude (VA) bands for quantitative fractography of small cracks. The CA bands consisted of 5000 high stress ratio CA cycles ($R = 0.77$) and the crack dimensions and growth in a single band were determined in the scanning electron microscope (SEM) after failure of the specimen. Approximately 500 blind holes were introduced on both sides of the plate material (1038 in total per specimen). The blind holes act as seeded defects for nucleation of surface cracks. The blind holes were made using an ultrashort pulse laser with a pulse length of 10 ps and a wavelength of 532 nm, operated at 10 kHz pulse repetition frequency. The holes were machined by scanning the laser in layers of several concentric circles. Multiple layers were used to machine the holes to a depth of about 80 μm. Rows of blind holes were made perpendicular to the loading direction and a spacing of 2 mm was used within a row. Separation of the rows in the direction of loading was 0.5 mm and adjacent rows were staggered by 1 mm to minimize interaction between growing cracks.

The crack depth (a) at the deepest point was used to calculate ΔK. The geometry factor β for the surface cracks has been determined with AFGROW software for the deepest point of the surface crack as fraction of the thickness (t) using the measured crack ratio (a/c, where c is half of the surface crack length) at different crack depths:

$$\beta = 0.5599(a/t)^3 - 0.0953(a/t)^2 + 0.2034(a/t) + 0.5687 \tag{6}$$

(only applicable for these seeded defects).

2.2.3. Smooth round stress-life coupons

Smooth round coupons for stress-life (*S-N*) testing were machined from 12.7 mm 7075-T7351 plate from the same mill. The coupons have a diameter of 3 mm and a reduced section length of 18 mm. The coupons have a stress concentration factor of unity ($K_t = 1$) and were polished to a roughness of $R_a < 0.2$ μm. A constant amplitude 25 Hz sinusoidal load was introduced by a servo-hydraulic test machine with a 100 kN load cell. A stress ratio, R, of 0.1 was applied.

S-N results are typically plotted with the cycles to failure on the horizontal axis and the stress on the vertical axis. However, since the cycles to failure is the outcome of the test and the maximum stress is the input value, in this paper scientific graphs are used where the independent variable is plotted on the horizontal axis and the dependent variable on the vertical axis. This is especially important when standard regression analysis is applied on the graph to obtain a power law exponent by minimizing the error between the model and the *dependent* variable. Plotting it vice versa results in different fitting parameters.

2.2.4. Tensile test specimens

Tensile tests were carried out on rectangular tensile specimens machined from M(T) specimens that were tested at a low maximum stress. The width of the specimens was 12.5 mm and the length of the reduced section was 82 mm. The thickness was equal to the plate thickness. The gauge length of the clip gauge was 50 mm and the tensile tests were performed under lab conditions on a test machine with a 100 kN load cell and a strain rate of 10^{-3} s^{-1}.

2.2.5. Fractography

A FEI field emission gun (FEG) SEM was used for fractography on all fatigue specimen types and energy dispersive analysis of X-rays (EDX) was used in the SEM to measure the composition of constituent particles on the fracture surface.

2.2.6. Fitting methodology

Making use of Eq. (2), the measured crack length, a, as a function of cycles, N, was fitted using the following equation:

$$a(N) = a(0) + \sum_{j=1}^{N} \frac{da}{dN_i}\left(\frac{\Delta K_j}{\Delta K_i}\right)^{n_i}, \tag{7}$$

where ΔK_j is the stress intensity factor range during the j^{th} cycle. For a constant stress range test ΔK_j is a function of the crack length prior to the j^{th} cycle, a_{j-1}. The pivot points in the FCGR curve are located at the coordinates (da/dN_i, ΔK_i) and the suffix i denotes the pivot point number. The pivot points correspond to the locations where the slope changes in the FCGR curve. In the fitting procedure the error between the measured crack lengths and the crack lengths calculated by Eq. (7) is minimized in a least square fitting procedure by changing the coordinates of the pivot points, the crack growth rates at the start and the end of the measurement, and the number of pivot points.

The pivot point coordinates fully define the slope between two pivot points. The crack growth rates at the start and the end of the measurement are required to define the slopes towards the first and after the last pivot point respectively.

The error, ϵ, between the model (Eq. (7)) and the measured a-N curve is calculated as follows:

$$\epsilon = \sum_{j \in V} \left(\tilde{a}_j - a_j \right)^2, \tag{8}$$

where a_j and $\tilde{a}_j$ are the measured and modelled crack lengths after the jth cycle respectively. The set V contains the cycles at which a measured crack length was stored.

When using Eq. (7), to find the crack growth rate at ΔK in between two pivot points, either of the adjacent pivot points may be used along with the slope at ΔK. For ΔK smaller than ΔK_1 the first slope n_1 is used with ΔK_1, for ΔK larger than ΔK_1, the slope n_{i+1} is used with ΔK_i.

3. Results

3.1. Long crack growth rate measurements – AA7075-T7351

Fig. 2 shows *a-N* curves of two specimens that were tested at $S_{max} = 80$ MPa and $R = 0.1$. The crack lengths measured with DCPD show good agreement with the optical crack length measurements. The noise on the DCPD measurement is clearly visible due to the large amount of data points. The scatter in the optical measurements is less clear due to the limited number of measurements. The DCPD measurements are used the obtain the FCGR by fitting the DCPD *a-N* curves with Eq. (7). Fig. 3 shows the normalized error between the DCPD *a-N* curve and the fit as a function of the number of slopes in the FCGR curve. Note that the number of slopes is one more than the number of transition points in a FCGR curve. The absolute value of the error depends on the number of data points, which depends on the test parameters. Therefore, the error of each specimen is normalized by the error at which the error does not significantly decrease anymore with increasing number of slopes. It is clear that the error does not decrease significantly when more than four slopes are used for specimen P1R2N2 and more than five for specimen P1R4N2. When less than four or five are used, the error between the fit and the measured a-N curve increases significantly. For specimen P2R3N1 the number of slopes is less obvious and four or five slopes can be used the fit the a-N curve of this specimen.

Fig. 4a shows the *a-N* curve of several specimens tested at different maximum stress and different stress ratios. The coloured dots represent the crack lengths measured with DCPD and the solid white line represents the best fit of Eq. (7) for each specimen. The black markers in the white line represent the transition points that correspond to the least number of transition points and slopes that are necessary to obtain a small error between the fit and the measured *a-N* curve. The white lines that represent the best fits run through the DCPD data points of all five specimens and show good agreement with the shape of the curves, also at small crack lengths.

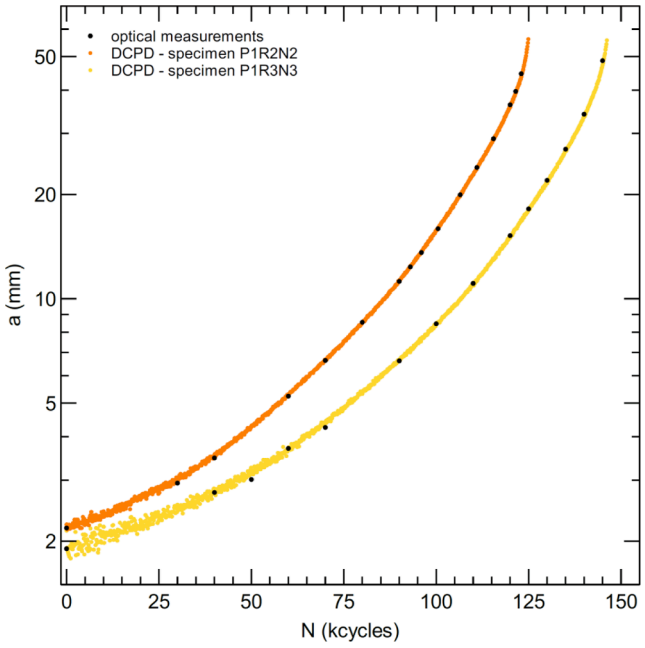

Fig. 2. Crack length vs. cycles (*a-N*) curve for two 7075-T7351 M(T) specimen tested at $S_{max} = 80$ MPa and $R = 0.1$. The coloured points indicate the crack length measurements using DCPD and the black dots indicate the optical crack length measurements.

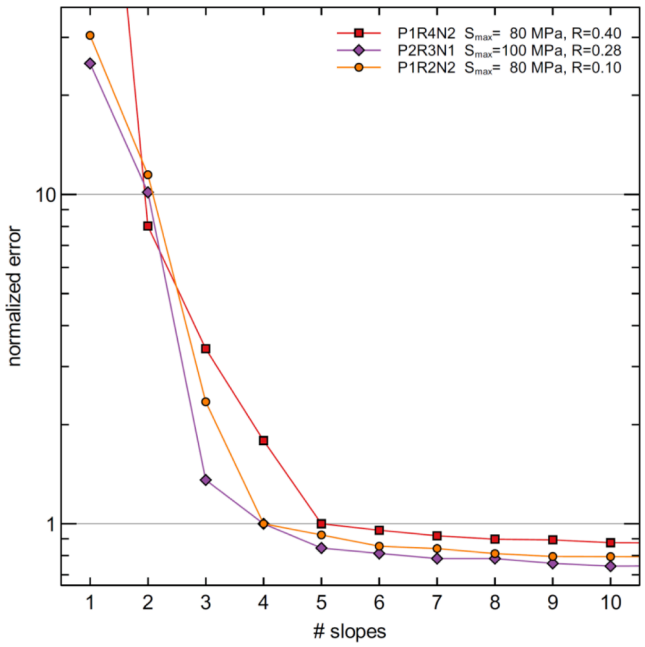

Fig. 3. Normalized error between the measured *a-N* curve and the fit using Eq. (7) as a function of the number of slopes in the FCGR curve.

Fig. 4b shows the resulting FCGR as a function of ΔK. Multiple changes to the slope can be observed and the transition from one slope to the next occurs at specific FCGR for all curves. The horizontal shift between the individual curves originates from the different stress ratios. Fig. 4b also shows the FCGR as a function of ΔK_{eff} and the shapes of the FCGR curves are similar such that they fall on top of each other when the FCGRs are plotted as a function of ΔK_{eff}. Since the FCGRs of specimens P2R2N1, P2R1N7 and P1R4N2 at the start of the test are less than that of specimens P1R2N2 and P2R3N1, they require an additional transition point and slope at the beginning of the FCGR curve. For the FCGR range between $3 \bullet 10^{-9}$ and 10^{-5} m/cycle a minimum of four transition points and five slopes are necessary to obtain accurate fit for all specimens. Since specimen P2R3N1 has a similar FCGR range as specimen P1R2N2, the same number of slopes has been used to fit the *a-N* curve.

The same fitting procedure can be used to fit the *a-N* data of a specimen tested with a very small stress range. Since the entire curve is fitted with Eq. (7), noise in the crack length measurement at very low FCGR ($<10^{-10}$ mm/cycle) does not influence the results. Fig. 5 shows that the *a-N* curve from a naturally increasing ΔK test with an initial FCGR of $5.8 \cdot 10^{-11}$ m/cycle can be fitted just as easily as *a-N* curves from specimens tested with higher stress ranges. The insert shows the result of the fit and at the start of the test the FCGR increases quickly with increasing ΔK until the slope changes at $8.7 \cdot 10^{-10}$ m/cycle. The exponent of the initial slope is 8.43 and failure of the specimen at the end of the curve occurs by net-section overload.

Fig. 6 shows the FCGR as a function of ΔK_{eff} for all specimens. This master curve consists of 54 M(T) specimens with 11 different maximum stresses and 13 different stress ratios. The master curve shows that there are five transition points and six slopes between FCGR of $5.8 \cdot 10^{-11}$ and 10^{-5} m/cycle, were region II is divided into regions IIa-IId.

Fig. 7 shows SEM images of the fracture surfaces at each region,

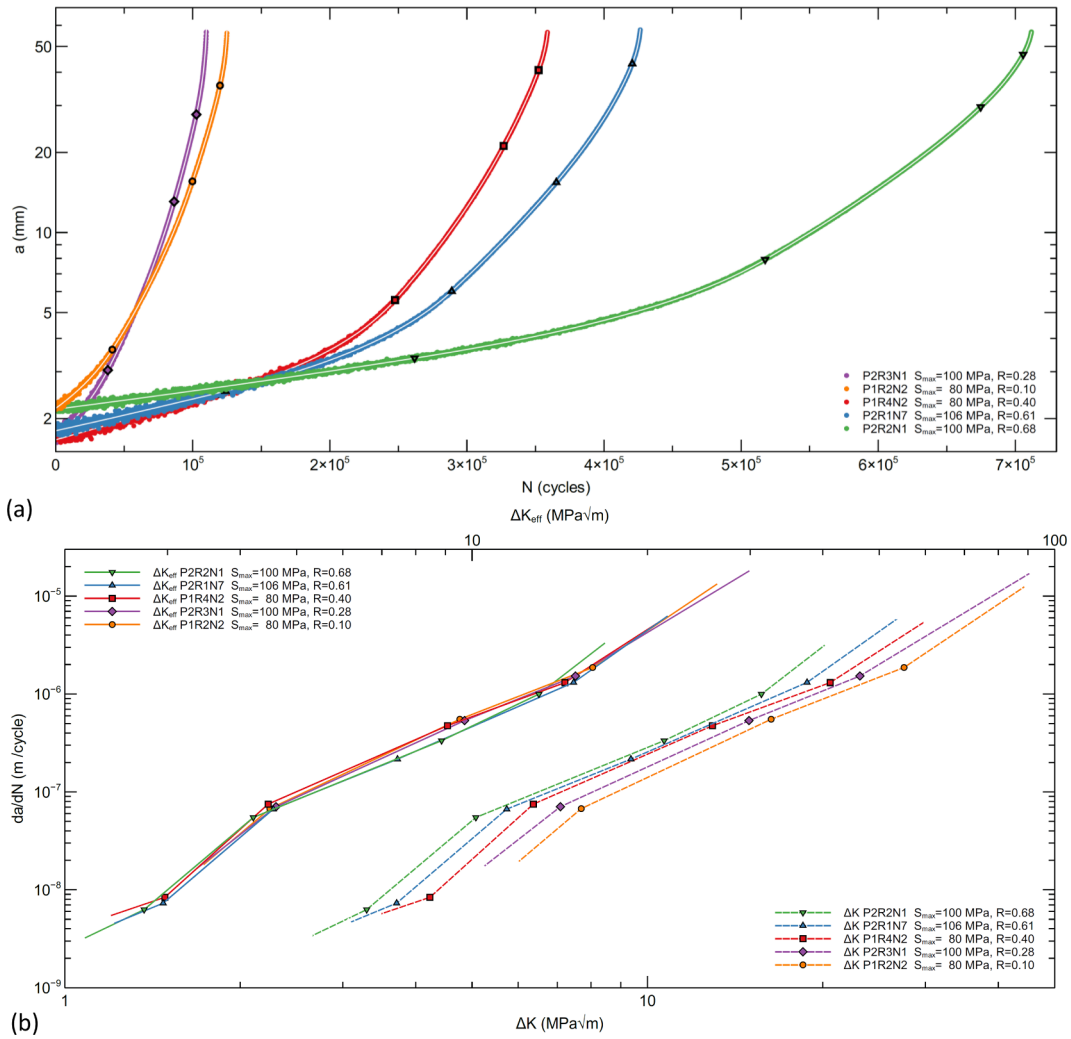

Fig. 4. (a) Crack length vs. cycles (a-N) curves for 7075-T7351 M(T) specimens tested at different S_{max} and R. The white lines indicate the fit using Eq. (7) and the black symbols in the white lines indicate transitions points. (b) FCGR as a function of ΔK and ΔK_{eff}. The transition points are indicated by the same symbols.

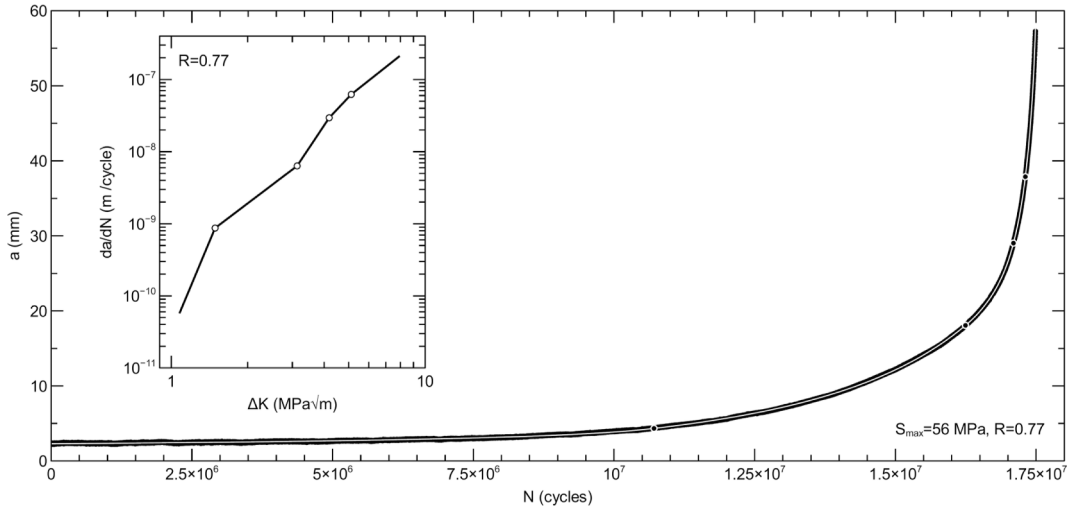

Fig. 5. a-N curve for an 7075-T7351 M(T) specimen tested at a small stress range. The insert shows the resulting FCGR from the fit using Eq. (7).

except for region IId. At region I the fracture surface has a facetted appearance. After the transition to region IIa the fracture surface is much smoother and there is little difference between the overall appearances of the subsequent region IIb. Region IIb does show some fissures with a spacing that is larger than the macroscopic FCGR. The fracture surface of region IIc is characterized by ductile striations with a striation spacing

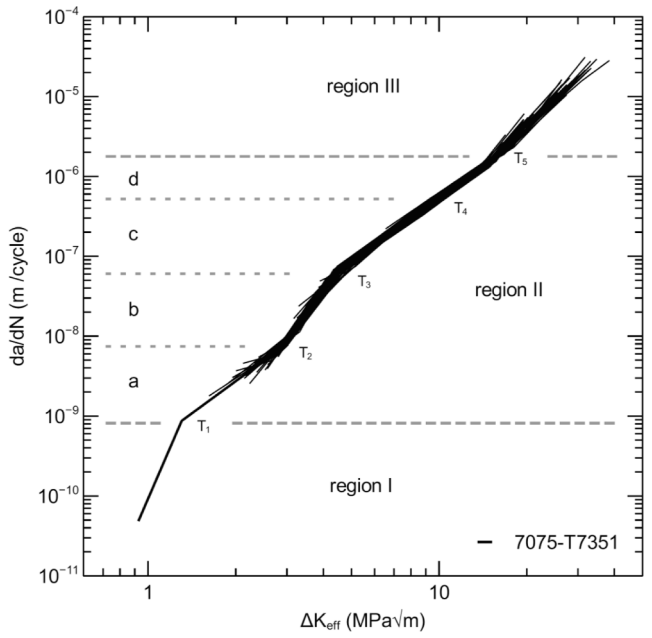

Fig. 6. FCGR master curve as a function of ΔK_{eff} with horizontal indications for the transitions between regions. The master curve consists of 54 specimens with 11 different maximum stresses and 13 different stress ratios.

that is equal to the macroscopic FCGR. The transition from region IIc to IId (T_4) is not characterized by a microscopic change in fracture surface appearance, but associated with a macroscopic change, i.e. the onset of shear lip development that leads to a fully slanted crack front as a result of a change in stress state from plane strain to plane stress [36]. The fracture surface of region III is characterized by microvoid nucleation and microcrack propagation ahead of the crack tip (see Fig. 7). Fig. 8 shows the transition crack lengths for T_3, T_4 and T_5 as determined by the fitting procedure as a function of the measured crack length at the onset of shear lip development. From the figure it is clear that shear lips develop at the crack length at which T_4 is reached or within 10 mm from that crack length.

3.2. Long crack growth rate measurements – Other materials and heat treatments

Specimens of 7075-O (annealed), 2524-T351 and 2524-O have been tested and the *a-N* curves have been fitted using Eq. (7). The number of pivot points corresponds to the minimum number that is necessary to obtain a low and constant error between the fit and the measured crack lengths. The fit of the *a-N* curve of the 7075-O, 2524-T351 and 2524-O specimens runs though the scatter band of the DCPD measurements, just as in Fig. 4a. Fig. 9a and b show the FCGR curves of 2524-T351 for two stress ratios. The FCGR curves of 7075-T7351 for the same stress ratio are shown for comparison. The negative slopes in the FCGR curves of 2524-T351 just before region III are the result of a decrease in FCGR due to widening of the shear lips, similar as region IId for 7075-T7351. For a stress ratio of 0.1 the FCGR of 2524-T351 is similar to 7075-T7351 between a ΔK_{eff} of 5.5 and 11 MPa$\sqrt{m}$. For $R = 0.46$ the overlap between FCGRs is much less and only present between a ΔK_{eff} of 8 and 11 MPa$\sqrt{m}$. Below $\Delta K_{eff} = 5.5$ MPa$\sqrt{m}$ for $R = 0.1$ and $\Delta K_{eff} = 8$ MPa$\sqrt{m}$ for $R = 0.46$ the FCGR of 2524-T351 is significantly<7075-T7351. Fig. 9c shows the FCGR for 7075 in the annealed and T7351-condition for $R = 0.1$. In region IIc the FCGR of the material in the O-condition is very similar as in the T7351-condition. However, after transition T_4 the slope for the O-condition is different compared with the T7351-condition. The slopes before and after T_5 are similar for the O-condition and these slopes are similar as the slope in region III for 7075-T7351. Fig. 9d shows the FCGR for annealed 7075 and 2524 material for $R = 0.46$ and the solution heat treated and aged conditions (T7351 and T351, respectively). For 7075 and $R = 0.46$ the O-condition gives similar FCGRs as the T7351-condition at region IIa. At region IIb and IIc the FCGR is less and at region IId and region III the FCGR is greater for the O-condition than for the T7351-condition. The similar and lower FCGR in the initial regions for the 7075-O specimens lead to a longer crack growth life for these M(T) specimens. For 2524 and $R = 0.46$ the O-condition gives FCGRs that are greater than for the T351-condition in all regions. The FCGRs for 2524-O are also greater than for 7075-O, except for the initial part of the curve. The FCGRs of these materials are overall quite similar, except for 2524-T351. The FCGR of 2524-T351, 7075-T7351 and 7075-O is about $4{\cdot}10^{-7}$ m/cycle at $\Delta K_{eff} = 9$ MPa$\sqrt{m}$ and $5{\cdot}10^{-7}$ m/cycle for 2524-O. This is in contrast to the difference in yield stress and ultimate tensile strength (UTS) between the materials. Table 1 shows the results of the tensile tests and the yield stress of 7075-T7351 is exactly a factor 4 greater than for 7075-O, while the overall FCGR of 7075-T7351 is similar to 7075-O.

Fig. 10a shows the FCGR curves of 7075-O for different maximum stresses up to the yield stress. There is an increase in the FCGR with increasing S_{max} for the same stress ratio ($R = 0.1$). Fig. 10b shows the FCGR curves of Inconel 601 for different maximum stresses up to the yield stress. A similar increase in FCGR with increasing S_{max} is observed for some part of the FCGR curve, while the FCGRs in and just prior to region III are similar for the different maximum stresses.

Fig. 11 shows the normalized FCGR as a function of the normalized maximum stress. The maximum stress is normalized by the yield stress and the FCGR is normalized by the FCGR at $\Delta K = 12$ and 33 MPa$\sqrt{m}$ for 7075-O and Inconel 601, respectively, and at the maximum stress equal to the yield stress. The results show that the effect of the maximum stress is limited up to about $S_{max}/S_y = 0.4$. For $S_{max}/S_y > 0.4$ the effect increases with increasing maximum stress-yield stress ratio. The FCGR for 7075-T7351 was arbitrarily scaled such that the normalized FCGR is 0.3 at $S_{max} = 80$ MPa ($S_{max}/S_y = 0.185$). For 7075-T7351 there is also a clear effect on the FCGR for $S_{max}/S_y > 0.3$. The results for plane strain conditions in 7075-T7351 are obtained at $\Delta K = 12$ MPa$\sqrt{m}$ and the results for plane stress conditions are obtained at $\Delta K = 20$ MPa$\sqrt{m}$. The effect of the maximum stress on the FCGR is more dominant in the plane strain conditions compared to the plane stress conditions.

3.3. Small crack growth rate measurements – AA7075-T7351

Fig. 12 shows the fatigue crack growth rate obtained from a small crack by alternating markerbands of constant amplitude ($R = 0.77$) and variable amplitude. The open dots represent FCGRs that are obtained from measuring the width of the CA bands, while the solid line represent the results from the crack length vs. cycles fit, similar as for the long crack specimens. The slope of the small crack in region I is 12.8, which is greater than the exponent of the long crack in region I ($n_1 = 8.43$). The slope in region IIa is slightly lower such that the two curves for small and long cracks merge near the transition to region IIb at a crack depth of about 2.2 mm.

The measured crack in Fig. 12 corresponds to the crack that was the largest when the specimen failed, i.e. the lead crack. For high maximum stresses typically multiple cracks develop in a specimen, but the depths of these cracks are different when the specimen fails by net-section overload. Apparently, the lead crack was able to grow to the largest size within the number of cycles to failure of the specimen.

Fig. 13 shows the crack growth rates as a function of the crack depth for multiple cracks on the same fracture surface of another small crack specimen. At the same crack depths and therefore the same stress intensity factor range, the FCGR of the lead crack is a factor 3 higher than that of the slowest crack on this fracture surface (see for example Fig. 14). The figure shows that there is a large spread in small crack growth rate at the same stress intensity factor range.

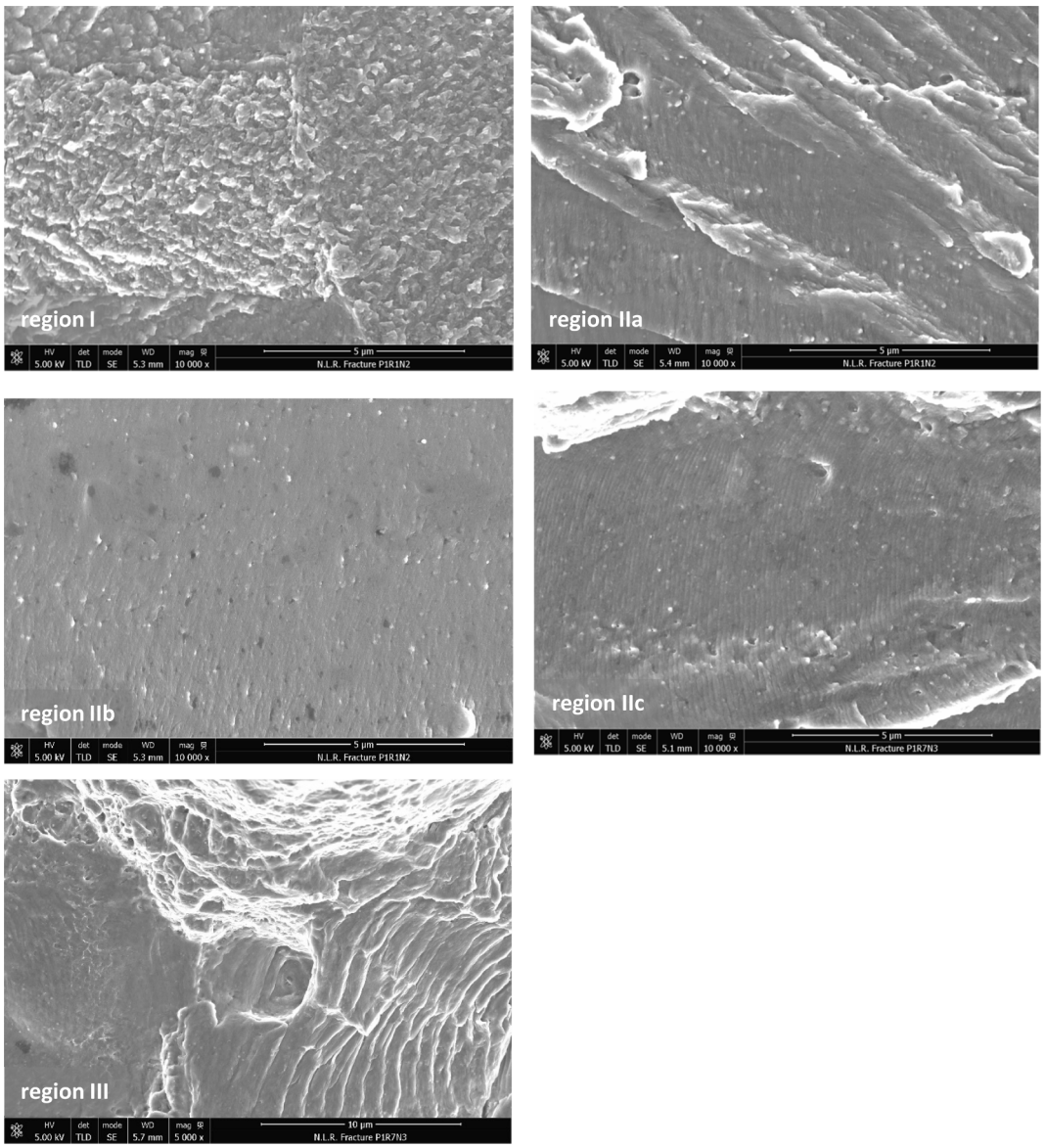

Fig. 7. Scanning electron microscope (SEM) images of at various regions of the FCGR curve. Crack growth direction is from right to left.

3.4. From crack growth rate to fatigue (crack growth) life

Fig. 15 shows *S-N* measurements for 7075-T7351 smooth round coupons and the calculated fatigue lives. The calculated fatigue life is determined by a crack growth calculation (CGC) from the initial crack depth to final failure using Eq. (7), an appropriate stress intensity factor (SIF) solution and pivot points that represent the small & long FCGR data. In the subsequent paragraphs the input for the CGC, i.e. initial crack depth, SIF solution, FCGR data and final failure criteria, are given.

3.4.1. Initial crack depth

In total 51 coupons were tested and fractography showed that 75% the fatigue cracks nucleated from constituent particles at the surface, 2% from internal pores and 23% from machine tool markings on the surface, even though the coupons were carefully machined and polished. From the constituent particles 5% failed from Al_2O_3 phases, 18% from Mg_2Si phases, 33% from Al-Fe-Si-Cr-Cu phases and 44% from Al_7Cu_2Fe phases. The chemical composition of the Al-Fe-Si-Cr-Cu phase resembles that of $Al_{12}Fe_3Si(Cr,Cu)$ and this phase has also been observed as nucleation site in 7475-T7351 [37].

The initial discontinuity dimensions (IDD) is defined as the actual dimensions of a single initial discontinuity. The Fe-containing particles at the surface are among the initial discontinuities from which fatigue crack nucleate and in this case the IDD is only quantified by the maximum depth of the particle as measured from the surface. The IDD of the majority of the Fe-containing phases ranges between 12 and 24 μm. The coupons with Fe-containing initial discontinuities that have an IDD in the order of 12 μm, 16 μm or 24 μm are separately indicated in Fig. 15. Fig. 16 shows an SEM image with an example of crack nucleation from an $Al_{12}Fe_3Si(Cr,Cu)$ constituent particle with an IDD of 17.7 μm.

3.4.2. SIF solution

Fractography also showed that the crack shape during crack growth is characterised by a circular crack front with the centre of the circle at the origin of the crack (at the surface of the specimen). Toribio et al. give an overview of SIF solutions for surface cracks in round bars subjected to tension loading [38]. The SIF solutions by Astiz and by Carpinteri for circular cracks in round bars are similar for $a/D \geq 0.1$, where a is the crack depth and D the diameter of the bar [39,40]. However, for $a/D \leq 0.1$ the two solutions start to deviate, see Fig. 17. The value of β goes to 0.74 for the solution of Carpinteri and to 0.35 for the solution of Astiz when a/D goes to zero [38]. However, the lowest a/D that was used by

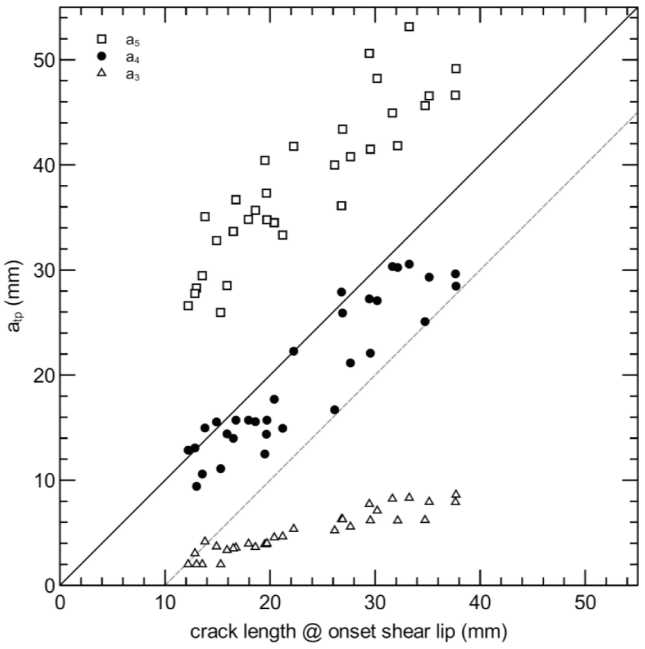

Fig. 8. Crack length at transitions T_3, T_4 and T_5 as a function of the measured crack length at the onset of the shear lips. The black line indicates $y = x$ and the grey dashed line indicates $y = x$-10.

Astiz to determine the SIF solution was 0.059, which resulted in a β of 0.59. This value is close to the value for a surface crack in a plate with $a/t = 0$ (see Eq. (6)). For $a \ll D$, it is expected that the influence of the curvature is very small and the SIF solution should approach the SIF solution of a surface crack in a plate. To avoid systematic errors between the determination of small crack FCGR measurements and the small crack growth calculations, a β value of 0.5687 was used for $a/D = 0$. This means that β is similar as the β for which the crack growth data was obtained and possible effects from the plane stress situation at the surface on the crack shape for $a \ll D$ is accounted for. When the crack depth increases, the influence of the curvature increases and the solution of Astiz is used. The following polynomial is used to describe β for the smooth round coupons and $0 < a/D \leq 0.6$:

$$\beta = 362.6\left(\frac{a}{D}\right)^6 - 683.6\left(\frac{a}{D}\right)^5 + 507\left(\frac{a}{D}\right)^4 - 174.3\left(\frac{a}{D}\right)^3 + 26.15\left(\frac{a}{D}\right)^2 - 0.02846\frac{a}{D} + 0.5687 \quad (9)$$

In the CGC the crack growth rate at the deepest point, i.e. the crack depth (a), is calculated and it is assumed that the circular shape of the crack is maintained for $a/D > 0.1$. For $a/D < 0.01$, Eqs. (6) and (9) are similar and the influence of the curvature of the bar diameter is small. This implies that the a/c ratio should be similar to that of small surface cracks, which is 1.29. For the constituent particle in Fig. 16 a crack depth of 17 μm and an a/c ratio of 1.29 characterizes the shape of the particle well. An a/c ratio of 1.29 also characterizes the shape of Fe-containing initial discontinuities in other specimens well. The initial crack depth and a/c ratio of a semi-elliptical crack that represents the shape and dimensions of an initial discontinuity is referred to as the representative initial discontinuity dimension (RIDD). The RIDD is used as initial crack depth, because the actual shapes of initial discontinuities cannot easily be used in the CGC. In the current CGC the a/c ratio is incorporated in the geometry factor, β, and the RIDD only consists of a crack depth. RIDD values of 12, 16 and 24 μm are used as initial crack depths in the CGC (a(0) in Eq. (7)).

3.4.3. FCGR data

Fig. 18 shows the small and long FCGRs as a function of ΔK_{eff} for the crack growth calculation. The effective stress intensity range is used to obtain the crack growth rates at $R = 0.1$, because measured FCGR data at $R = 0.1$ is not available for all regions. For the small FCGR the accurate FCGR from the small crack fit of Fig. 12 has been used and the slope in region IIa was extended up to the intersection with the available $R = 0.1$ long crack growth data in Fig. 6. This intersection defined the second transition point (T_2). From that point onwards the available $R = 0.1$ long crack data was used for the small FCGR. For the long FCGR the slope in region I and first transition point (T_1) from Fig. 5 and Fig. 6 were used. The slope in region IIa is determined by transition points T_1 and T_2. From transition T_2 onwards the available $R = 0.1$ long crack data was used for the long FCGR. The dashed cyan line that represents the long FCGR does not run through the middle of the master curve, because the available $R = 0.1$ long crack data is located in the upper range of the master curve (see Fig. 10 for available $R = 0.1$ long crack data and subtle differences with $R = 0.46$ long crack data).

3.4.4. Final failure criteria

The CGC is ended when the net-section stress reaches the ultimate tensile strength (UTS) of the material or when the maximum SIF reaches the fracture toughness (K_{IC}). All specimens in the calculations failed by net-section overload and the final crack depths in the calculations corresponded well with the measured crack depths (see Fig. 19).

There is a good agreement between the calculated fatigue lives and the measured fatigue life of the coupons for $310 > S_{max} > 375$ MPa when the small FCGR data and three appropriate RIDDs are used (see Fig. 15). When the long FCGR data is used the prediction overestimates the fatigue life for all three RIDDs.

4. Discussion

4.1. Long crack growth rate behaviour

4.1.1. Transitions

Fig. 6 shows that in total there are 6 different slopes and hence 5 transition points in the FCGR curve of 7075-T7351. The first three transitions occur at $9{\cdot}10^{-10}$, $8{\cdot}10^{-9}$ and $7{\cdot}10^{-8}$ m/cycle, which correspond to the three transitions at $1{\cdot}10^{-9}$, $1{\cdot}10^{-8}$ and $6.4{\cdot}10^{-8}$ m/cycle observed by Newman et al. for AA7075-T6 and Yoder et al. for several 7XXX-series aluminium alloys (see Fig. 1) [16,18]. The first transition at $9{\cdot}10^{-10}$ m/cycle also corresponds to the transition that occurred at a FCGR of $1{\cdot}10^{-9}$ m/cycle for steel from various sources and denoted as the transition from region I to Region II [9]. The fourth transition occurs at about $5{\cdot}10^{-7}$ m/cycle and the fifth between 1 and $2{\cdot}10^{-6}$ m/cycle. The fifth transition corresponds to the fourth one indicated by Newman et al. to denote the transition from region II to region III [18]. Hence, the pivot points correspond to the transitions that are classically observed in these alloys.

4.1.2. Micro-mechanisms

Many authors indicate that crack propagation is governed by different micro-mechanisms and result in different fatigue crack growth rates, i.e. different slopes in the FCGR curve [9,11–17,41–46]. The transition from one micro-mechanism to the next occurs when the monotonic or cyclic plane strain plastic zone dimensions become equal to characteristic microstructural dimensions [9,11–13,16,17,43]. For example, Yoder *et al.* indicated that each change in slope is associated with a specific microstructural feature that can serve as a barrier to slip-band transmission, e.g. the transition from region I to region II is controlled by mean free path between the dispersoid particles [16]. Wanhill indicated for AA2024 that the first transition occurs when the cyclic plastic zone dimensions are equal to the mean planar distance between dispersoids, the second transition occurs when the cyclic plastic zone dimensions are equal to the subgrain and dislocation cell sizes and the third occurs when the monotonic plastic zone dimensions are equal

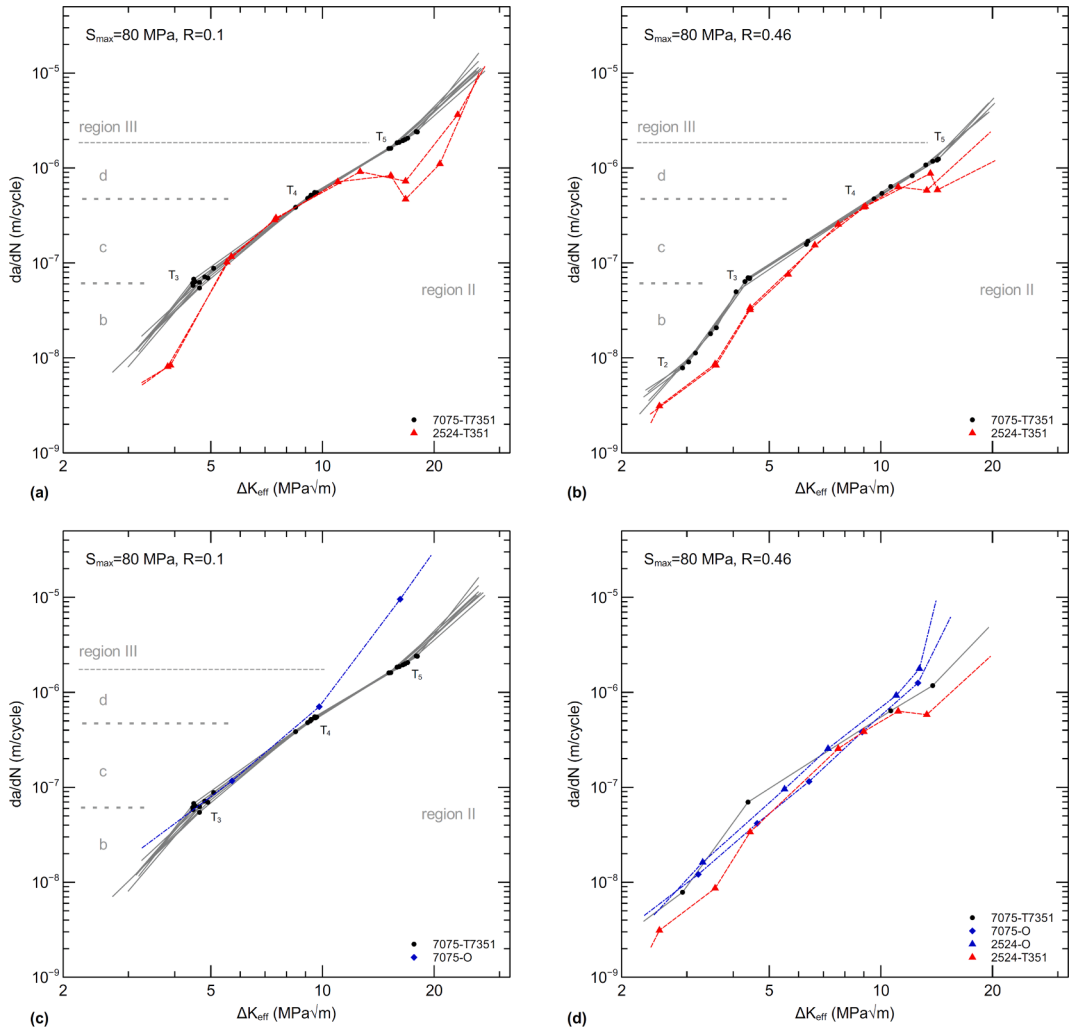

Fig. 9. FCGR curves of 7075-T7351 and 2524-T351 for (a) $R = 0.1$ and (b) $R = 0.46$. (c) FCGR curves of 7075-T7351 and 7075-O for $R = 0.1$. (d) FCGR curves of 7075-T7351, 7075-O, 2524-T351 and 2524-O for $R = 0.46$. For clarity only one curve of 7075-T7351 is shown in (d).

Table 1
Mechanical properties of the materials and heat treatments.

Material	S_y (MPa)	UTS (MPa)	Strain at UTS (%)
7075-T7351	433	498	8.0
2524-T351	337	444	18.6
7075-O	108	213	13.5
2524-O	97	217	14.8
Inconel 601	284	653	47.6

to the grain dimensions [17].

The change in micro-mechanism is usually reflected by a change in the fracture surface topography [11–15,41–46]. Fig. 7 shows similar results, i.e. specific fracture surface appearances for specific regions in the FCGR curve, and it can be concluded that the different stages of crack growth are related to different micro-mechanisms of crack growth and to different regions in the FCGR curve.

4.1.3. Plasticity

The average long crack exponent of regions I, II and III as obtained from Fig. 6 are 8.43, 3.2 and 4, respectively. The average exponent for region II, i.e. the Paris regime, is in the middle of the range of Paris slopes indicated by Fleck et al. for aluminium alloys [2]. Fleck et al. also show that the Paris slope ranges from 2.5 for ductile pressure vessel steel & stainless steels to 50 for brittle engineering ceramics. Similar results are reported by Ritchie [47]. This general trend indicates that plasticity at the crack tip can have an influence on the slope of the FCGR curve.

The fracture surface of 7075-T7351 has a facetted appearance in region I (see Fig. 7). The facetted appearance corresponds to crystallographic crack growth in stage I, where crack growth occurs predominantly along slip bands in the slip system experiencing the maximum resolved shear [48]. However, at a macroscopic scale the crack front runs across many grains and remains in a plane normal to the uniaxial applied stress, unlike the typical small stage I crack that grows under 45° angles. Hence, this type of crack growth has been referred to as stage I-like propagation [49]. The facetted appearance during stage I-like propagation indicate that there is limited plasticity. Discrete dislocation modelling of a plane strain crack subject to remote mode I cyclic loading under small-scale yielding show that two distinct regimes of behaviour emerge naturally from the modelling: a steeply rising slope in region I followed by a more gradual slope in the Paris regime [50]. The change in slope is due to the increased plastic dissipation at the higher ΔK values [50]. This corresponds to the slopes observed in Fig. 6 and the fractography in Fig. 7.

Zuidema et al. observed a change in FCGR slope for AA 2024-T3 and 7075-T6 when shear lips develop and concluded that the shear lips are not responsible for the change in slope, but an underlying mechanism that changes when the stress state changes from plane strain to plane stress [36]. The change in stress state from plane strain to plane stress at

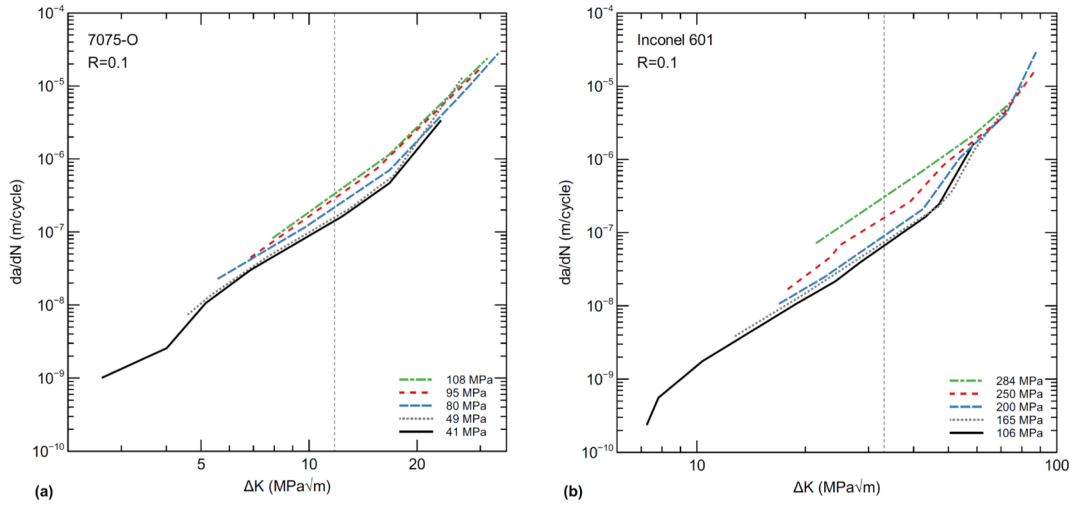

Fig. 10. FCGR as a function of ΔK for (a) 7075-O and (b) Inconel 601 at $R = 0.1$ and various maximum stresses. The vertical dotted line indicates the ΔK at which the FCGR are normalized in Fig. 11.

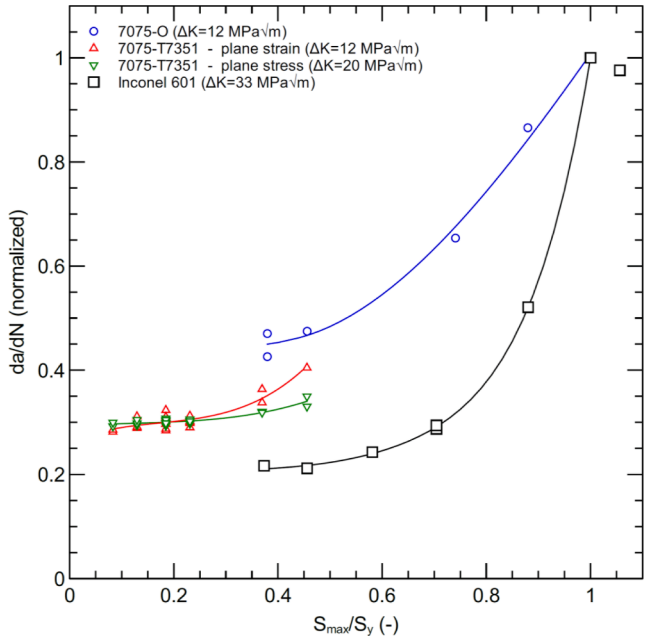

Fig. 11. Normalized FCGR as a function of normalized S_{max} for different materials and $R = 0.1$. The S_{max} and the FCGR at 12 and 33 MPa$\sqrt{m}$ for 7075-O and Inconel 601, respectively, are normalized by the material's yield stress and the FCGR at those ΔK values for the specimens tested with a maximum stress equal to the yield stress. The FCGR for 7075-T7351 was arbitrarily scaled such that the normalized FCGR is 0.3 at $S_{max} = 80$ MPa ($S_{max}/S_y = 0.185$). The curves are best fit by eye.

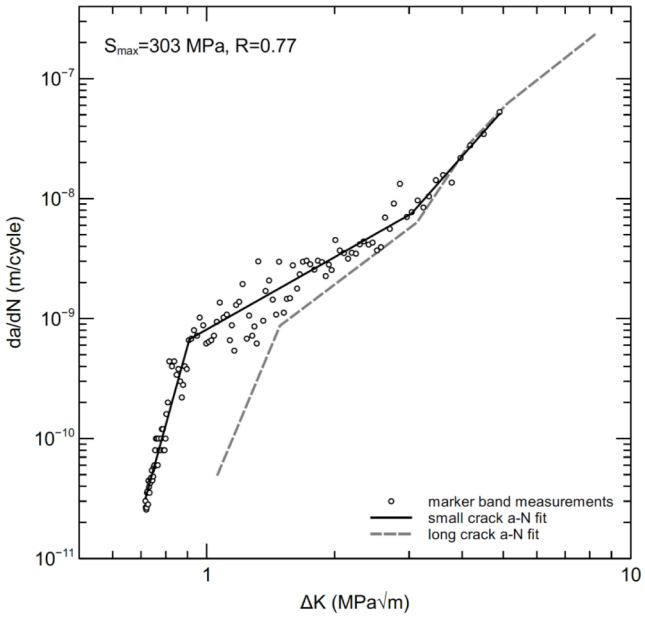

Fig. 12. Small crack growth measurements and small crack depth vs. cycles fit. The long crack *a-N* fit corresponds to the 7075-T7351 M(T) specimen in Fig. 5.

T_4 results in an increase in plasticity around the crack, because the plastic zone size in plane stress is greater than the size in plane strain [51–55].

Griberg et al. stated that for all engineering alloys the Paris slope increases with decreasing temperature, when the effect of environment is omitted by testing in vacuum or inert gas, and it was concluded that the decreasing plastic zone size with decreasing temperature is responsible for the change in slope [56–60].

From the above it is concluded that a change in the micro-mechanism of crack growth is most likely associated with a change in plasticity or plastic dissipation at the crack tip and a resulting change in FCGR slope. This gives a physical explanation for the presence of multiple slopes in the FCGR curve and justifies the use of Eq. (7) to model the fatigue crack growth.

4.1.4. Novel fitting methodology

It is expected that the least number of slopes that are necessary to describe the FCGR curve is equal or close to the number of micro-mechanisms of crack growth. There is a clear difference in fracture surface topography between stage I, which has a facetted appearance, and stage IIa. In stage IIc, the fracture surface is characterized by ductile striations with a striation spacing that is equal to the macroscopic FCGR. Therefore, stages I, IIa and IIc appear to have different micro-mechanisms. However, it is possible that a certain slope in the FCGR curve is a transition zone between two micro-mechanisms. For example, region/stage IIb does not show a different fracture surface topography than region/stage IIa and it could be that region IIb is a transition zone between regions IIa and IIc, instead of a transition point (see Fig. 7).

However, a change in slope does not have to be characterized by a

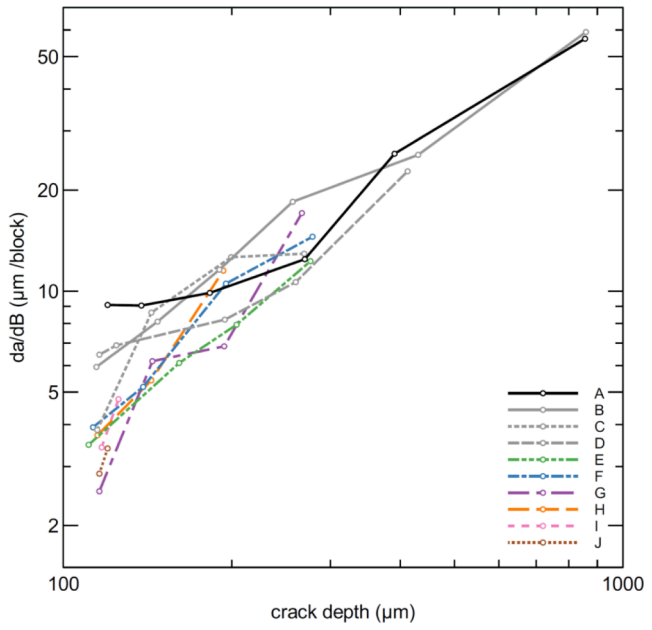

Fig. 13. Crack growth rate per CA + VA spectrum block as a function of the crack depth for several surface cracks on one fracture surface. The legend indicates the crack designation arranged from maximum (A) to minimum crack depth (J) at failure. The open dots represent individual measurements of the CA + VA spectrum block width at similar crack depths and the connecting lines are shown for clarity (the curves are not obtained by crack length fitting).

microscopic change in fracture surface appearance. Fig. 8 shows that the transition (T_4) from region IIc to IId is associated with a macroscopic change, i.e. the onset of shear lip development that leads to a fully slanted crack front. From Fig. 8 it is clear that shear lips develop at the crack length at which T_4 is reached or within 10 mm from that crack length. Zuidema et al. indicated that the onset of shear lip development in 2024 and 7075 depends on the environment; a more aggressive environment shifts the transition to larger crack lengths, which could explain the scatter in Fig. 8 [36,61]. For region III it is likely that the microvoid nucleation and microcrack propagation ahead of the crack tip results in higher crack growth rates compared to crack growth rate at the same SIF range in the absence of microvoids.

Fig. 3 shows that the error between the measured crack lengths and the fit increases rapidly when not enough slopes are used and that there is no significant decrease when more slopes are used. It is expected that the transition from one slope to the next does not occur at a single point, but more gradually. It is likely that the slightly lower error from additional pivot points originates from allowing a gradual transition from one region to another. The stable error that is obtained when a sufficient number of pivot points is used indicates that there is a good correlation between the fit and the raw *a-N* data. The additional pivot points are apparently not necessary to describe the FCGR curve more accurately. The pivot points should approach the general location of the transitions in the FCGR curve when a minimum number of pivot points is used to reach a stable error. The resulting FCGR curves are suitable for accurate reconstruction of the measured *a-N* curves. This implies that the crack growth rate between the pivot points can be described by power law behaviour. The power law behaviour can be used in all three regions as shown by the accurate fits in Fig. 4 and Fig. 5. This was shown earlier for individual or adjacent regions by [3–8,18].

The advantage of directly fitting the *a*-N curve is that i) it is not necessary to fit noisy FCGR data with a model, because an exact description of the FCGR curve is known from the fit of the *a-N* curve, ii) an accurate reconstruction of the a-N curve from the obtained FCGR data is possible. The method can be applied on naturally increasing ΔK testing with FCGR starting in region I, which avoids the problems associated with load shedding to obtain FCGR in region I. The method can also be used on *a-N* curves of small cracks to obtain accurate small crack FCGR data (see Fig. 12) and on *a-N* curves of variable amplitude (VA) loading to obtain VA FCGRs [62].

4.2. Small crack growth rate behaviour

Short cracks are faster than expected from long crack growth rate data [63]. For long cracks the width and length are much larger than the microstructural length scales and generally linear elastic fracture mechanics (LEFM) can be applied [64]. Short cracks are small in one dimension, but large in another, such as a through crack that nucleates from a notch [64]. Small cracks are small in all dimensions and in literature distinctions are made between microstructurally, mechanically and physically small cracks to explain why small cracks can grow at higher growth rates than long cracks [64–68]. Microstructurally small cracks (MSC) have dimensions comparable to the scale of the microstructure and the plastic zone size is less than important microstructural features such as the distance between dispersoids, the subgrain and dislocation cell sizes or the grain size [64]. The growth of MSC is highly affected by local microstructural characteristics and the environment [65,69–72]. The crack is able to grow in a preferential location and orientation and the crack front covers only one or several grains, so that the crack growth is not averaged with less advantageously oriented grains [64]. Hence, Ritchie and Lankford state that inhomogeneous sampling of the microstructure probably plays a major role in the distinction between small cracks and short through-thickness cracks, whose crack fronts must encompass many grains [64].

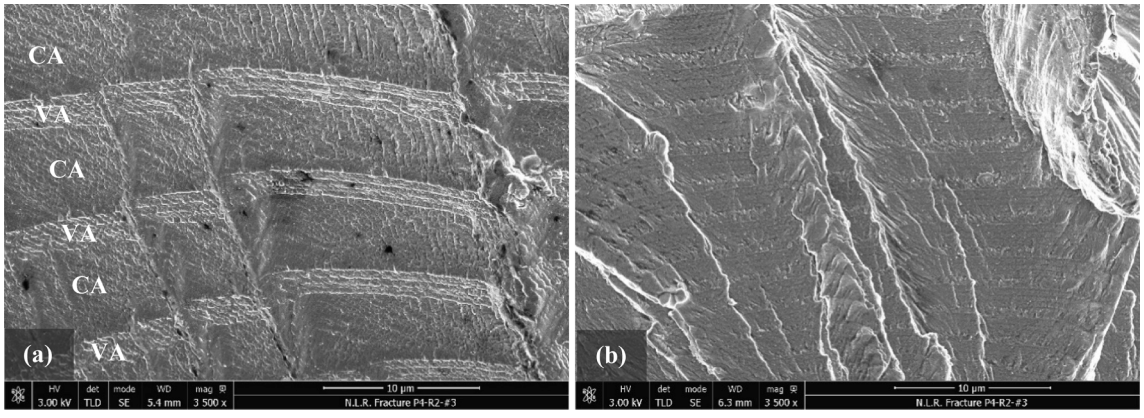

Fig. 14. SEM images of the CA + VA spectrum block growth rate at a crack depth of 120 μm for (a) the second largest and (b) the smallest crack at failure. These cracks correspond to crack B and crack J in Fig. 13, respectively.

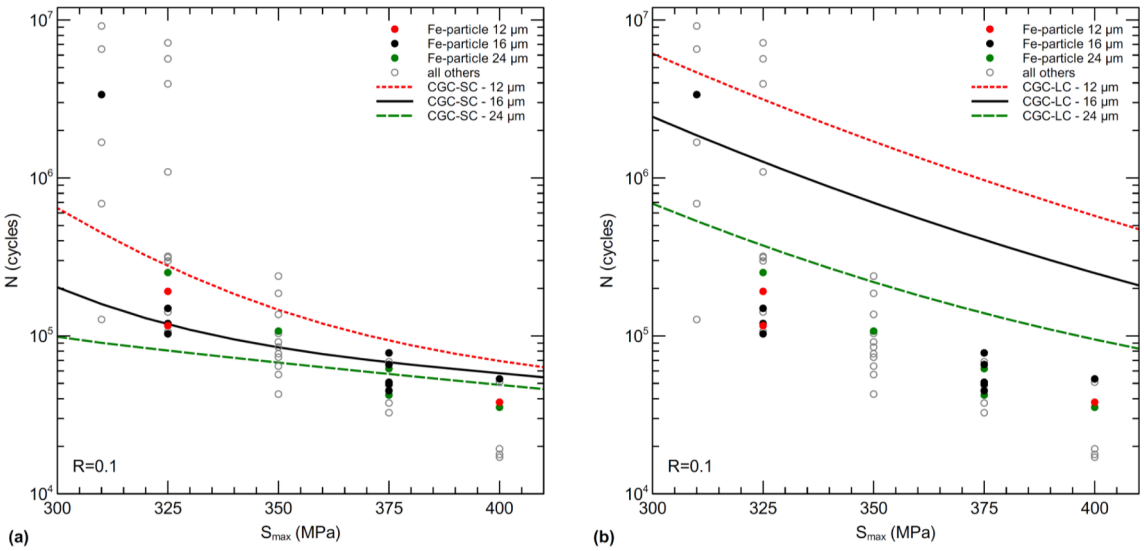

Fig. 15. Measured fatigue life as a function of the maximum stress and predicted fatigue life using (a) small crack (SC) and (b) long crack (LC) growth rate data. The filled dots represent specimens that nucleated a crack from Fe-containing constituent particles with IDD in the order of 12 µm, 16 µm or 24 µm. The lines indicate the crack growth calculation (CGC) for initial crack depths of 12 µm, 16 µm or 24 µm.

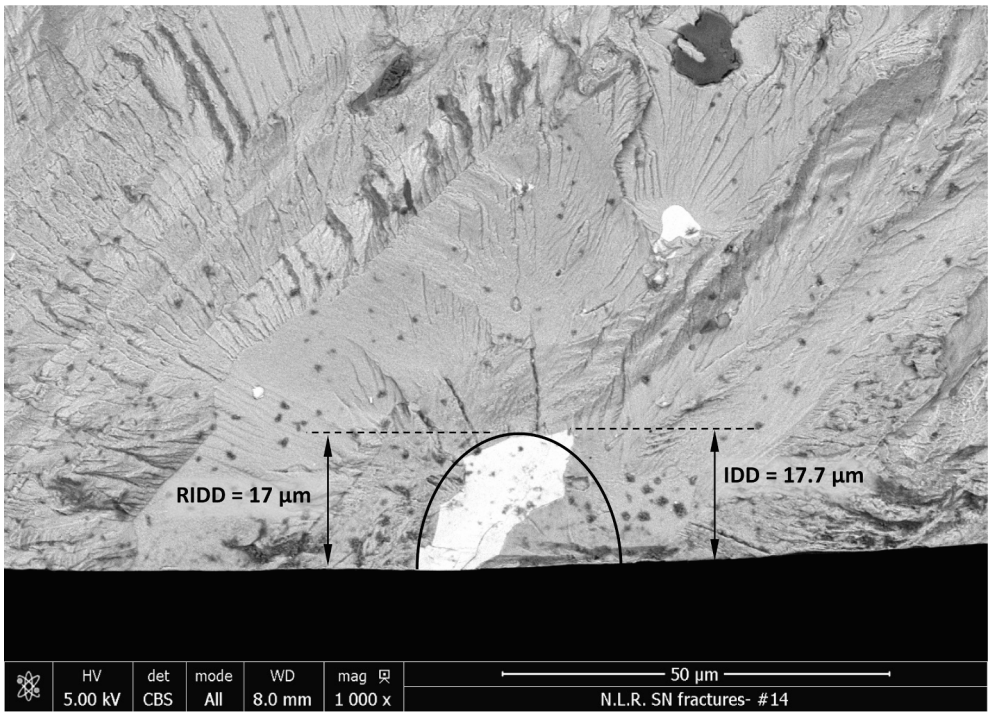

Fig. 16. SEM image of an $Al_{12}Fe_3Si(Cr,Cu)$ constituent particle from which crack nucleation occurred. The black ellipse has a depth of 17 µm and an a/c ratio of 1.29.

Fig. 6 shows that all long FCGR curves collapse on a master curve for ΔK_{eff} and it is equivalent to state that the transition from one region to another occurs at a specific ΔK_{eff} or a specific FCGR. Fig. 12 shows the evolution of the FCGR as a function of ΔK for an MSC and a long crack. The results were both obtained with constant ΔS testing, therefore with naturally increasing ΔK testing and with the same stress ratio ($R = 0.77$). Hence, the figure would look the same if the FCGR was plotted as a function of ΔK_{eff}. One might argue that that crack-closure is not present in the MSC, but it is also expected that limited crack closure is present in the long crack for $R = 0.77$. Even when no closure is assumed for the MSC and closure is assumed for the long crack, there is still a gap in ΔK_{eff} at the transition T_1. The MSC of Fig. 12 shows faster FCGR compared to the long crack, which is consistent with literature. The slopes of the MSC in region I and II are different compared to the long crack. However, Fig. 12 shows that the transition from region I to region II for the MSC occurs at the same FCGR as for the long crack. The FCGR of the MSC is obtained by the small crack length fit using Eq. (7) and hence the transition point from region I to region II can be determined accurately. Since the transition from region I to region II (T_1) for small and long cracks occurs at a specific FCGR, it is concluded that the transition from region I to region II is governed by the FCGR instead of the crack driving force, ΔK_{eff}. Hence, the transitions between different regions in Fig. 6 and other figures are indicated horizontally.

Fig. 13 shows a large variability in FCGR for small cracks near the

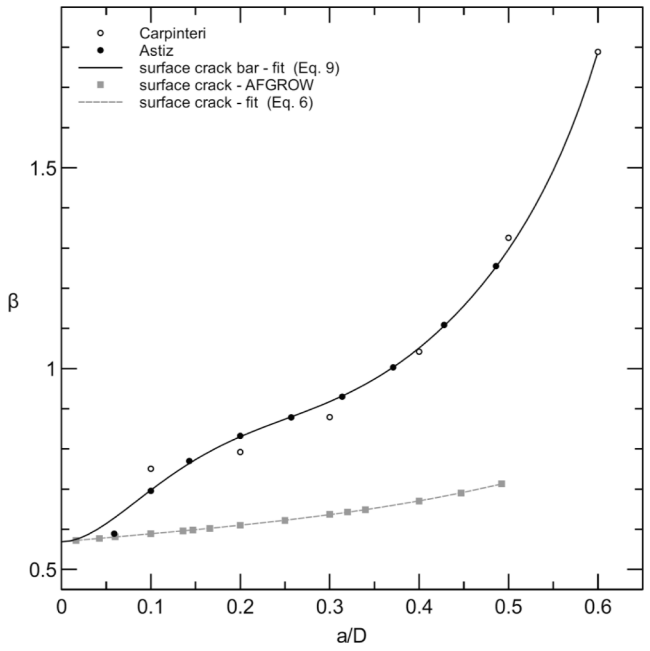

Fig. 17. Geometry factor, β, for a round bar as a function of the surface crack depth to diameter ratio. For the surface crack in a rectangular cross-section, the thickness T is used for D.

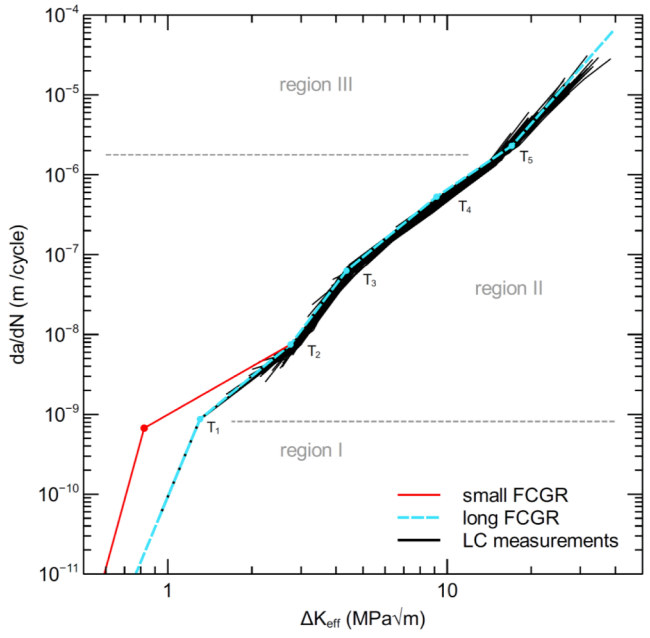

Fig. 18. Small and long FCGR that is used in the CGC. The 7075-T7351 long FCGR master curve from Fig. 6 is shown for comparison.

transition from region I to region II. The variability decreases with increasing crack depth. It also shows that the lead crack of that specimen, i.e. the crack that was largest when the specimen failed, was the fastest of 11 cracks at a crack depth of 110 μm. It appears that the lead crack is already growing in region II while other cracks still have a steep slope between the first data points and are likely still growing in region I. Markerbands could only be measured accurately for all cracks from 110 μm crack depth onwards. Therefore, it is unclear whether this crack was also the fastest directly after nucleation. However, when the specimen failed it was overall the fastest in crack nucleation and crack growth. For cracks with multiple measurements in region I, the slopes between these

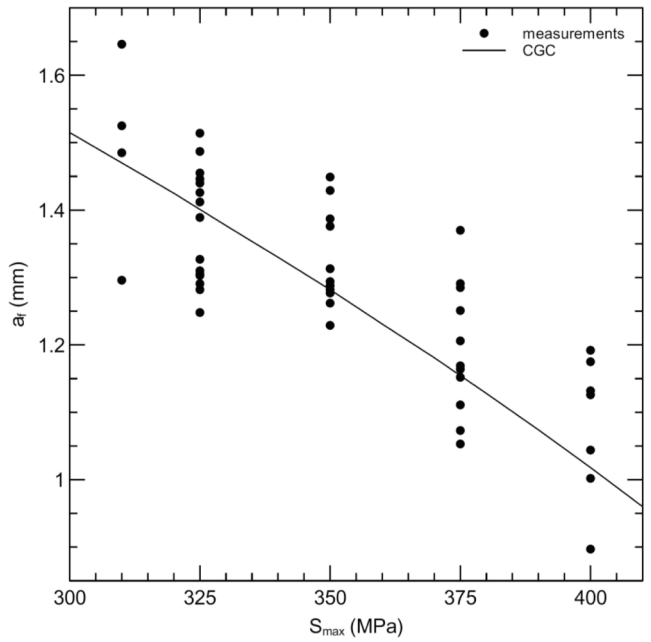

Fig. 19. Crack depth at failure as a function of the maximum stress for the smooth round S-N coupons ($R = 0.1$).

data points are similar and also similar to the region I slope for the MSC in Fig. 12. The variability in region I is mainly caused by vertical translation of the FCGR curves. Since these cracks are all present on one fracture surface, the applied maximum stress and stress ratio was equal for these cracks. The crack that failed the specimen, i.e. the lead crack, grows to the final size in a limited number of CA + VA spectrum blocks and most life is spend when the lead crack is still very small (<0.5 mm). The distance between the blind, laser drilled holes in a row is 2 mm and it is expected that the interaction between cracks is limited. All cracks nucleated from blind, laser drilled holes, with the same geometry and hence the same geometry factor, β. Therefore, ΔK_{eff} is the same for these cracks for a given crack depth.

The long crack growth rates originate from through cracks in M(T) specimens. The crack in the M(T) specimen spans many grains in the 6.35 mm thickness of the plate and the location of the crack is predetermined by the location of the 3 mm long EDM notch. In stage I-like propagation the crack front runs across many grains and remains in a plane normal to the uniaxial applied stress. Hence, the crack growth rate of long cracks is an average over many cycles and many grains. The MSC propagate in only a few grains and many crack nucleation and propagation locations are present in a single specimen. At locations suitable for crack growth, much higher crack growth rates are possible as observed in Fig. 13. Once it is assumed that the transitions between regions are controlled by the FCGR in conjunction with the microstructural features, a change in ΔK_{eff} at which the transition occurs becomes the direct result of the presence of variability in MSC FCGR. If the microstructure is locally very beneficial for a small crack growing in stage I this will give high FCGRs. Since the MSC that are measured are always the fastest ones, the transition T_1 will shift to smaller values compared to the long cracks. Hence, for a transition from region I to region II at a specific FCGR, the difference between the region I FCGR of fast small cracks and average long cracks result in an apparent shift in ΔK_{eff} at which the transition occurs. This indeed points to inhomogeneous sampling as the reason for the lower threshold for small cracks as indicated by Ritchie and Lankford [64].

In literature this shift is often referred to as the shift in $\Delta K_{\text{threshold}}$. Kitagawa and Takahashi were the first to show that the threshold for small cracks actually decreased with decreasing crack length and the threshold stress approached the smooth bar fatigue limit for MSC

[65,73]. The Kitagawa-Takahashi diagram also addresses the higher crack growth rate for small cracks by an empirical relationship that shifts the threshold for small initial crack lengths, but it does not give a physical explanation. Adjustments to the diagram have been proposed by El Haddad et al. by adding a fictitious crack length to the physical crack length [74] and Murakami et al. by replacing the crack length by the square root of the area [75,76]. However, it is still deterministic in a sense that cracks either grow or do not grow depending on which side of the curve they are located based on their length or area and stress. However, there is enough evidence that small cracks do lead to failure, while they are in the no-grow area and vice versa [77]. Addressing the problem with probabilistics with proper distributions for the initial crack length and for the variability in small crack growth rate in region I as indicated by Fig. 13 should be able to account for this.

4.3. Maximum stress-yield stress ratio phenomenon

The maximum stress-yield stress ratio phenomenon results in an increase in FCGR and the increase can be different for different regions (see Fig. 10 and Fig. 11). The increase in FCGR with increasing maximum stress for the same ΔK and stress ratio could result from an increase in plastic deformation in the material. If so, more energy is available for crack growth and a proper parameter of similitude would in this case be the range of the J-integral, ΔJ, instead of ΔK. However, Fig. 10 shows that for Inconel 601 the phenomenon is restricted to a specific region in the FCGR curve and it is almost not present near and in region III. Therefore, the phenomenon is different for different regions and this is not expected when ΔJ should replace ΔK as the parameter of similitude. Fig. 11 also shows small differences between 7075-T7351 tests at 36 MPa and 106 MPa maximum stress, while these stresses are well below the yield stress and the entire plate is already subjected to many load cycles during pre-cycling. Hence, it is expected that there is limited plasticity in the material during the FCGR test (except for the plastic zone at the crack tip). The phenomenon can also not be explained by increasing influence of plasticity at higher maximum stress-yield stress ratio, because the Manson-Coffin relationship in general and for 7075 in particular shows that the presence of plasticity at maximum stress-yield stress ratio>0.75 increases the number of cycles to failure for a given total strain range compared with the same total strain range comprising from elastic strain [78]. Fig. 11 shows that the phenomenon is already present at a maximum stress-yield stress ratio of 0.38 for 7075-T7351 and the phenomenon reduces the number of cycles to failure by increased crack growth rate in contrast to the influence of plasticity in the Manson-Coffin relationship. The phenomenon was also observed in 2024-T3 between maximum stress-yield stress ratios of 0.19 and 0.38 [79]. A decrease in crack-opening stress with increasing maximum stress as determined by a plasticity induced crack closure model with constraint factor α was used to explain the increase in FCGR [79].

Fig. 11 shows that the influence of the maximum stress increases with increasing maximum stress-yield stress ratio. The curve is horizonal at small values of the normalized $S_{\max}$ indicating that there is no significant influence of $S_{\max}$ on the FCGR as a function of ΔK. In that case, for a given stress ratio, the FCGR is a function of the crack length and the square of the maximum stress, when $m_i = n_i/2$:

$$\frac{da}{dN} \propto \left(S_{max}^2 a^1\right)^{m_i}, \tag{10}$$

If δ is defined as the ratio between the exponent on maximum stress and crack length, then δ is 2 for Eq. (10) and the SIF. However, at high values of normalized $S_{\max}$ the FCGR increases with increasing $S_{\max}$ for a given ΔK. When the relative increase in FCGR between two maximum stresses for a given ΔK is equal to the relative increase in stress to the power m, then there is a cubed relationship between $S_{\max}$ and the crack length ($S_{max}^3 a$, where δ is 3). For that condition the vertical difference between the FCGR curves due to the maximum stress-yield stress ratio phenomenon is equal to a horizontal shift of the curve when the maximum stress is incorporated within the brackets of Eq. (10). Near the yield stress the relative increase in FCGR is greater than the relative increase in stress to the power m and δ becomes>3. As such, δ is a function of the derivative of the curves in Fig. 11.

For M(T) specimens that are tested with a high $S_{\max}$ the FCGR at the start of the test is in region IIc or d and most cycles that are accumulated during the test are by crack growth in regions IIc and d. For 7075-T7351 the exponents n_i in those regions are close to two. Hence, exponents m_i are close to unity and for a constant stress range during the test the crack growth is exponential. Hence, for high maximum stresses where the exponents m_i are close to unity and δ is 3 or larger, the Frost-Dugdale relationship.

$$\frac{da}{dN} \propto S_{max}^3 a \tag{11}$$

is more appropriate [80,81]. It can therefore be concluded that for long cracks an FCGR equation based on the SIF is more appropriate for $S_{\max} \leq 0.6S_y$ and the Frost-Dugdale type equation is more appropriate for high maximum stresses. Similar conclusions were drawn for variable amplitude fatigue where Amsterdam found a δ of 2.12 for 7075-T7351 and reference stresses between 75 and 140 MPa [62]. Huynh et al. found a δ of 3.13 for 7050-T7451 and reference stresses between 270 and 450 MPa [82]. Molent and Jones extended the work to a number of materials, spectra and stress concentrations and entitled it as the stress-cubed (or cubic) rule [83,84]. Although the Frost-Dugdale is appropriate in some cases, for most maximum stresses δ is not equal to 3. For small cracks the power law exponents n_i of regions I and IIb are not close to two and the Frost-Dugdale relationship is not appropriate anymore.

For *S-N* coupons the IDD are usually very small and coupons are usually tested at high maximum stresses to induce failure by fatigue. Therefore, the maximum stress-yield stress ratio phenomenon becomes important for fatigue crack growth in these specimens. Although Fig. 13 shows that there is variability in stage I FCGR for MSCs, which indicates that inhomogeneous sampling at small length scales is the cause for the apparent shift in ΔK at the transition, it is possible that the maximum stress-yield stress ratio phenomenon is very dominant in stage I FCG and contributes to the differences between MSC that are tested at high maximum stress-yield stress ratios and long cracks that are tested at small ratios. Therefore, it cannot be excluded that the higher FCGR of MSC in region I is partly due to maximum stress-yield stress ratio phenomenon.

4.4. From crack growth rate to fatigue (crack growth) life

The fatigue life was calculated from an RIDD to failure using Eq. (7) and immediate crack growth was assumed without a nucleation phase. Jin et al. concluded that fatigue cracks in 7075-T651 nucleated at pre-cracked Al_7Cu_2Fe constituent particles when the specimen was loaded in the L direction and crack initiation from this phase has been observed for high strength aluminium alloys by many authors [63,85–90]. Barter et al. expected immediate fatigue crack growth from these pre-cracked particles under high cyclic stress and observations on crack nucleation from corrosion pits indicated that crack nucleation from less sharp stress concentrator occurs essentially immediately upon the application of cyclic loading [90–93]. Therefore, it is expected that crack growth from pre-cracked or cracked Fe-containing particles occurs from the first loading cycle for highly loaded smooth *S-N* specimens. If additional cycles for fatigue nucleation were included, the total cycles to failure would increase. The predicted fatigue lives at maximum stresses >350 MPa are greater than the experimental lives (see Fig. 15). Adding additional cycles for nucleation would only increase the discrepancy between the predicted and experimental fatigue lives.

Forman was one of the first to investigate the use of fracture mechanics for crack nucleation from initial discontinuities [94]. El Haddad

et al. incorporated short crack effects to the fracture mechanics by adjusting the $\Delta K_{threshold}$ to predict the fatigue life of smooth and notched specimens [95]. Newman et al. used a multilinear FCGR curve to calculate the *S-N* curve [19,96–98]. Small crack growth rate data was used to determine the slope in region I and the transition from region I to region II (see Fig. 1). A similar approach is followed here, with the exception that power law behaviour is assumed a priori and the transition points and slopes in the FCGR curve are determined accurately by fitting the crack length vs. cycles curves of small and long cracks directly. Fatigue cracks that nucleate from initial discontinuity states, e.g. corrosion pits, fractured constituent particles or pores, usually start as an MSC [64]. When the MSC grows, and the dimensions become larger than the microstructural features, the MSC evolves into a physical small crack before it eventually becomes a long crack [64]. Fig. 1 shows that similar slopes are used in region IIa for small and long cracks in 7075-T6. Fig. 12 shows that the small and long FCGR merge near transition T_2 and this behaviour is used in Fig. 18 to model the evolution of an MSC to a long crack in 7075-T7351.

Goto and Nisitani indicated that the *S-N* curve is determined by the small crack growth rate and relate the slope of the *S-N* curve to the slope of small crack growth rate in carbon steel [99]. Tanaka and Akiniwa used the *S-N* curve to derive the crack growth rate in region I and II for internal crack growth from inclusions [100]. They indicate that for internally nucleated fatigue with long lives, most of the fatigue life is spent in crack growth in Region I and they used power law behaviour with different exponents to describe the crack growth rate in regions I and II. However, due to the multilinear FCGR curve, the FCGR variability in region I and the maximum stress-yield stress ratio phenomenon, it is not possible to obtain one or multiple FCGR slopes from the *S-N* curve when the IDD and final crack length are the only points that are known from the *a-N* curve. Multiple data points in the *a-N* curve that fall into the same crack growth region have to be present to obtain information on slopes in the FCGR curve. Fig. 15 shows that there is a gradual change in the slope of the predicted fatigue life, where the slope at high maximum stress is related to the average exponent in region II and the slope at lower maximum stress increased towards the exponent in region I. Although the predicted curve approaches the region I FCGR slope, it is not equal to the region I curve because the cycles to failure is the result of crack growth in region I and region II. The fatigue life prediction at the maximum stress of 325 MPa, which is close to the 303 MPa at which the small FCGR data was determined, shows good agreement with the measured lives. However, at $S_{max} > 375$ MPa the predicted fatigue life is greater than the measured fatigue lives and it is expected that proper incorporation of the maximum stress-yield stress ratio phenomenon is necessary to accurately predict the fatigue life for smooth and notched coupons.

5. Conclusions

Fatigue crack growth occurs through different micro-mechanisms and this leads to different slopes in the FCGR curve. To accommodate for multiple slopes in the FCGR curve, mathematical pivot points are introduced in the Paris equation. The introduction of pivot points and by assuming power law behaviour in all regions of the FCGR curve it is possible to directly fit the crack length vs. cycles (*a-N*) curve to obtain the FCGR as a function of ΔK. The fitting method results in accurate FCGR curves that are suitable for reconstruction of the measured *a-N* curves of 7075-T7351.

The ability to accurately fit *a-N* curves for cracks growing in region I confirms that region I long crack growth rate is governed by power law behaviour and provides a method for obtaining accurate region I fatigue crack growth rates for naturally increasing ΔK testing. The same applies for cracks growing in regions II and III, indicating that crack growth is governed by power law behaviour in all regions. Accurate small crack FCGR can be obtained by applying the method to naturally increasing ΔK testing of microstructurally small cracks. The accurate small crack growth rate measurements have been used to calculate the fatigue life from initial discontinuity dimensions and the results correspond roughly to the fatigue life results that are experimentally obtained for smooth *S-N* specimens. Using only accurate long crack FCGR to calculate the fatigue life from initial discontinuity dimensions results in unconservative fatigue lives.

It is shown that the new fitting methodology can be applied to:

1. Different alloys.

The resulting FCGR curves show specific changes in the location of transition points and adjacent slopes for changes in alloy composition and heat treatments.

2. Small cracks.

The results for small cracks show that for constant ΔS testing and therefore naturally increasing ΔK testing there is still a difference between small and long crack growth rate. The results also show that crack growth rate of small cracks in region I can vary significantly. However, the transition from region I to region II occurs at a specific fatigue crack growth rate for both small and long cracks. The variation in crack growth rate for region I combined with the transition from region I to region II at a specific fatigue crack growth rate results in an apparent shift in ΔK at the transition. This points at inhomogeneous sampling as one of the reasons for the lower threshold of small cracks. Another cause for the differences between the FCGR of small and long cracks could be the maximum stress-yield stress ratio phenomenon, which could be dominant in region I.

3. Long cracks.

The results on long cracks show that the FCGR increases with maximum stress for a given ΔK and stress ratio when the maximum stress approaches the yield stress. The phenomenon is referred to as 'the maximum stress-yield stress ratio phenomenon' and can vary per FCG region. The increase in FCGR with maximum stress indicates that the ratio between the exponent on stress and crack length, δ, is not constant. As a result the Paris equation is applicable rather at low maximum stress, while the Frost-Dugdale equation is more applicable at high maximum stress and long cracks. This phenomenon becomes especially important in the case of fatigue life testing and predictions, where the initial crack lengths are usually small and maximum stresses are high. It is also the most likely cause for the discrepancy between the fatigue life prediction and experimental results at maximum stresses that approach the yield stress.

Author contribution

EA was responsible for the set-up and execution of experimental work, data analysis and theoretical development and writing of the manuscript. MN was responsible for data analysis architecture and initial algorithms for data processing. JWW performed further development of the algorithms for data processing and processed the crack length vs. cycles data. JDH performed review & editing of the manuscript.

Declaration of Competing Interest

The authors declare that they have no known competing financial interests or personal relationships that could have appeared to influence the work reported in this paper.

Acknowledgement

The authors would like to thank Marcel Bos for his comments on the manuscript. This work was part of a public-private partnership project called "Prediction of fatigue in engineering alloys" (PROF). Financial

contributions from the Netherlands Ministry of Economic Affairs and Climate Policy, through TKI-HTSM and the Materials Transition Programme, the Netherlands Ministry of Defence, GKN Fokker, Embraer, Airbus, Wärtsilä and Lloyd's Register are gratefully acknowledged. Scientific discussions with Tim Janssen (GKN Fokker), Giorgia Aleixo, Marcelo de Barros (Embraer), Derk Daverschot (Airbus), Jiajun Wang, Aarif Zaheer (Wärtsilä), Weihong He, Li Xu (Lloyd's Register), Jesse van Kuijk and René Alderliesten (TU Delft) during the project are highly acknowledged.

References

[1] Paris PC, Erdogan F. A critical analysis of crack propagation laws. J Basic Eng 1963:528–33.
[2] Fleck NA, Kang KJ, Ashby MF. The cyclic properties of engineering materials. Acta Metall Mater 1994;42:365–81. https://doi.org/10.1016/0956-7151(94)90493-6.
[3] Paris PC. The fracture mechanics approach to fatigue. Proc. of the 10th Sagamore Army Materials Research Conference, Syracuse University Press; 1964, p. 107–32.
[4] Laird C, Smith GC. Crack propagation in high stress fatigue. Phil Mag 1962;7:847–57. https://doi.org/10.1080/14786436208212674.
[5] McEvily AJ, Boettner RG. On fatigue crack propagation in F.C.C. metals. Acta Metall 1963;11(7):725–43.
[6] Liu HW, Iino N. A mechanical model for fatigue crack propagation. Proceedings of the 2nd Int. Conference on Fracture, Chapman and Hall; 1969, p. 812-824 (paper 71).
[7] Yokobori T, Kurbayashi H, Kawagishi M, Takeuchi N. Studies on the initiation and propagation of fatigue crack in tempered martensitic high strength steel by plastic replication method and scanning electron microscope. Rep Res Inst Struct Fracture 1971;7:1–23.
[8] Yokobori T, Nanbu M, Takeuchi N. Observations of initiation and propagation of fatigue crack by plastic replication method. Rep Res Inst Strength Fract Mater 1969;5:1–17.
[9] Radhakrishnan VM. Quantifying the parameters in fatigue crack propagation. Eng Fract Mech 1980;13:129–41. https://doi.org/10.1016/0013-7944(80)90048-X.
[10] Wilhem DP. Investigation of cyclic crack growth transitional behavior. Fatigue crack propagation, ASTM 415. ASTM Int 1967:363–80.
[11] Yoder GR, Cooley LA, Crooker TW. Quantitative analysis of microstructural effects on fatigue crack growth in widmanstätten Ti-6A1-4V and Ti-8Al-1Mo-1V. Eng Fract Mech 1979;11:805–16. https://doi.org/10.1016/0013-7944(79)90138-3.
[12] Wanhill R, Galatolo R, Looije C. Fractographic and microstructural analysis of fatigue crack growth in a Ti-6Al-4V fan disc forging. Int J Fatigue 1989;11:407–16. https://doi.org/10.1016/0142-1123(89)90179-5.
[13] Wang H. A study on the change of fatigue fracture mode in two titanium alloys. Fatigue Fract Eng Mater Struct 1998;21:1077–87. https://doi.org/10.1046/j.1460-2695.1998.00095.x.
[14] Mills WJ, Brown CM. Fatigue fracture surface morphology for alloy 718. Superalloys 718, 625, 706 and various derivatives, TMS; 2001.
[15] Kunz J, Nedbal I, Siegl J, Pártl O. Detailed study of stage II of fatigue crack propagation. Workshop 93, Prague: Czech Technical University; 1993, p. 193–4.
[16] Yoder GR, Cooley LA, Crooker TW. On microstructural control of near-threshold fatigue crack growth in 7000-series aluminum alloys. Scr Metall 1982;16:1021–5. https://doi.org/10.1016/0036-9748(82)90448-3.
[17] Wanhill RJH. Low stress intensity fatigue crack growth in 2024–T3 and T351. Eng Fract Mech 1988;30:233–60. https://doi.org/10.1016/0013-7944(88)90227-5.
[18] Newman Jr. JC, Wu XR, Venneri SL, Li CG. Small-crack effects in high-strength aluminum alloys - A NASA/CAE cooperative program; 1994.
[19] Newman Jr JC, Wu XR, Swain MH, Zhao W, Phillips EP, Ding CF. Small-crack growth and fatigue life predictions for high-strength aluminium alloys. Part II: crack closure and fatigue analyses. Fat Frac Eng Mat Struct 2000;23:59–72. https://doi.org/10.1046/j.1460-2695.2000.00242.x.
[20] Forman RG, Kearney VE, Engle RM. Numerical analysis of crack propagation in cyclic-loaded structures. J Basic Eng 1967;89:459. https://doi.org/10.1115/1.3609637.
[21] Forman RG, Mettu SR. Behavior of Surface and Corner Cracks Subjected to Tensile and Bending Loads in Ti-6Al-4V Alloy. Houston, Texas: NASA; 1990.
[22] Hartman A, Schijve J. The effects of environment and load frequency on the crack propagation law for macro fatigue crack growth in aluminium alloys. Eng Fract Mech 1970;1:615–31. https://doi.org/10.1016/0013-7944(70)90003-2.
[23] ASTM: E647-15. Test Method for Measurement of Fatigue Crack Growth Rates. West Conshohocken, PA: ASTM International; 2015. Doi: 10.1520/E0647-15E01.
[24] Amsterdam E. On the validity of the Paris equation. AIAC 2017: Innovation into Aerospace Future, Melbourne, Vic.: 2017, p. 1–6.
[25] Amsterdam E, Nawijn M. Fatigue tests for alloys. Aerospace Testing International 2018;Showcase 2018:16–20.
[26] Amsterdam E, Grooteman F. The influence of stress state on the exponent in the power law equation of fatigue crack growth. Int J Fatigue 2016;82:572–8. https://doi.org/10.1016/j.ijfatigue.2015.09.013.
[27] McCartney LN, Irving PE. Comments on: "A correlation for fatigue crack growth rate". Scr Metall 1977;11:181–3. https://doi.org/10.1016/0036-9748(77)90048-5.
[28] Yokobori T. Fundamentals and methodologies of fracture. Japanese Edition. Tokyo: Wanami Shoten; 1974.
[29] Tanaka K, Masuda C, Nishijima S. The generalized relationship between the parameters C and m of Paris' law for fatigue crack growth. Scr Metall 1981;15:259–64. https://doi.org/10.1016/0036-9748(81)90340-9.
[30] Iost A, Lesage J. On the existence of a pivot point for stage II fatigue crack growth. Eng Fract Mech 1990;36:585–96. https://doi.org/10.1016/0013-7944(90)90114-V.
[31] Iost A. The effect of load ratio on the m−ln C relationship. Int J Fatigue 1991;13:25–33. https://doi.org/10.1016/0142-1123(91)90125-I.
[32] Iost A. Temperature dependence of stage II fatigue crack growth rate. Eng Fract Mech 1993;45:741–50. https://doi.org/10.1016/0013-7944(93)90062-W.
[33] J. R. Davis & Associates, ASM International, editors. Aluminum and aluminum alloys. Materials Park, OH: ASM International; 1993.
[34] Schijve J. Shear lips on fatigue fractures in aluminium alloy sheet material. Eng Fract Mech 1981;14:789–800. https://doi.org/10.1016/0013-7944(81)90091-6.
[35] Schijve J. Fatigue crack closure, observations and technical significance. Delft University of Technology; 1986.
[36] Zuidema J, Veer F, Van Kranenburg C. Shear lips on fatigue fracture surfaces of aluminum alloys. Fatigue Fract Eng Mater Struct 2005;28:159–67. https://doi.org/10.1111/j.1460-2695.2004.00837.x.
[37] Ohnišťová P, Píška M, Dluhoš J, Horníková J, Šandera P, Petrenec M. A Study of Crack Initiation Mechanism in the Aluminum Alloy 7475–T7351 when Tensile Loading. Procedia Struct Integrity 2019;23:469–74. https://doi.org/10.1016/j.prostr.2020.01.131.
[38] Toribio J, Álvarez N, González B, Matos JC. A critical review of stress intensity factor solutions for surface cracks in round bars subjected to tension loading. Eng Fail Anal 2009;16:794–809. https://doi.org/10.1016/j.engfailanal.2008.06.023.
[39] Astiz MA. An incompatible singular elastic element for two- and three-dimensional crack problems. Int J Fract 1986;31:105–24. https://doi.org/10.1007/BF00018917.
[40] Carpinteri A. Elliptical-arc surface cracks in round bars. Fat Frac Eng Mat Struct 1992;15:1141–53. https://doi.org/10.1111/j.1460-2695.1992.tb00039.x.
[41] Forsyth PJE. A two stage process of fatigue crack growth. Crack Propagation: Proceedings of Cranfield Symposium, Cranfield: Her Majesty's Stationery Office; 1961, p. 76–94.
[42] Forsyth PJE. Fatigue damage and crack growth in aluminium alloys. Acta Metall 1963;11:703–15. https://doi.org/10.1016/0001-6160(63)90008-7.
[43] Stofanak RJ, Hertzberg RW, Leupp J, Jaccard R. On the cyclic behavior of cast and extruded aluminum alloys. Part B: Fractography Eng Fracture Mech 1983;17(6):541–54.
[44] James LA, Mills WJ. Effect of heat-treatment and heat-to-heat variations in the fatigue-crack growth response of alloy 718. Eng Fract Mech 1985;22:797–817. https://doi.org/10.1016/0013-7944(85)90109-2.
[45] Mercer C, Soboyejo ABO, Soboyejo WO. Micromechanisms of fatigue crack growth in a forged Inconel 718 nickel-based superalloy. Mater Sci Eng, A 1999;270:308–22. https://doi.org/10.1016/S0921-5093(99)00214-2.
[46] Mercer C, Soboyejo ABO, Soboyejo WO. Micromechanisms of fatigue crack growth in a single crystal Inconel 718 nickel-based superalloy. Acta Mater 1999;47:2727–40. https://doi.org/10.1016/S1359-6454(99)00123-8.
[47] Ritchie RO. Mechanisms of fatigue-crack propagation in ductile and brittle solids. Int J Fract 1999;100:55–83. https://doi.org/10.1023/A:1018655917051.
[48] Pang H, Reed P. Effects of microstructure on room temperature fatigue crack initiation and short crack propagation in Udimet 720Li Ni-base superalloy. Int J Fatigue 2008;30:2009–20. https://doi.org/10.1016/j.ijfatigue.2008.01.001.
[49] Petit J, Kosche K. Stage I and stage II propagation of short and long cracks in Al-Zn-Mg alloys. Short Fatigue Cracks, London: Mechanical Engineering Publications; 1992, p. 135–51.
[50] Deshpande VS, Needleman A, Van der Giessen E. Discrete dislocation modeling of fatigue crack propagation. Acta Mater 2002;50:831–46. https://doi.org/10.1016/S1359-6454(01)00377-9.
[51] Irwin GR. Fracture mode transition for a crack traversing a plate. J Basic Eng 1960;82:417–23. https://doi.org/10.1115/1.3662608.
[52] Dugdale DS. Yielding of steel sheets containing slits. J Mech Phys Solids 1960;8:100–4. https://doi.org/10.1016/0022-5096(60)90013-2.
[53] Ewalds HL, Wanhill RJH. Fracture mechanics. 1st ed. Delft: Edward Arnold and Delftse Uitgevers Maatschappij; 1984.
[54] Lopez-Crespo P, Camas D, Antunes FV, Yates JR. A study of the evolution of crack tip plasticity along a crack front. Theor Appl Fract Mech 2018;98:59–66. https://doi.org/10.1016/j.tafmec.2018.09.012.
[55] Matvienko YG. The effect of out-of-plane constraint in terms of the T-stress in connection with specimen thickness. Theor Appl Fract Mech 2015;80:49–56. https://doi.org/10.1016/j.tafmec.2015.05.007.
[56] Liaw PK, Fine ME, Kiritani M, Ono S. The effect of temperature on the fatigue crack propagation rate in aluminum. Scr Metall 1977;11:1151–5. https://doi.org/10.1016/0036-9748(77)90325-8.
[57] Grinberg NM. The effect of vacuum on fatigue crack growth. Int J Fatigue 1982;4:83–95. https://doi.org/10.1016/0142-1123(82)90064-0.
[58] Serdyuk V, Grinberg N. The plastic zone and growth of fatigue cracks in magnesium MA12 alloy at room and low temperatures. Int J Fatigue 1983;5:79–85. https://doi.org/10.1016/0142-1123(83)90058-0.

[59] Verkin BI, Grinberg NM, Serdyuk VA, Yakovenko LF. Low temperature fatigue fracture of metals and alloys. Mater Sci Eng 1983;58:145–68. https://doi.org/10.1016/0025-5416(83)90041-1.
[60] Grinberg NM. Physical base for the fatigue crack growth parameters and their change at low temperature. Basic mechanisms in fatigue of metals. Prague: /Elsevier; 1988. p. 255–62.
[61] Vogelesang LB, Schijve J. Environmental effects on fatigue fracture mode transitions observed in aluminium alloys. Fat Frac Eng Mat Struct 1980;3(1):85–98.
[62] Amsterdam E. Effect of Crack Length and Reference Stress on Variable Amplitude Fatigue Crack Growth Rate. In: Niepokolczycki A, Komorowski J, editors. ICAF 2019 – Structural Integrity in the Age of Additive Manufacturing, Cham: Springer International Publishing; 2020, p. 539–50. Doi: 10.1007/978-3-030-21503-3_43.
[63] Pearson S. Initiation of fatigue cracks in commercial aluminium alloys and the subsequent propagation of very short cracks. Eng Fract Mech 1975;7:235–47. https://doi.org/10.1016/0013-7944(75)90004-1.
[64] Ritchie RO, Lankford J. Small fatigue cracks: A statement of the problem and potential solutions. Mater Sci Eng 1986;84:11–6. https://doi.org/10.1016/0025-5416(86)90217-X.
[65] Suresh S, Ritchie RO. Propagation of short fatigue cracks. Int Metals Rev 1984;29:445–75. https://doi.org/10.1179/imtr.1984.29.1.445.
[66] Chan KS, Lankford J, Davidson DL. A comparison of crack-tip field parameters for large and small fatigue cracks. J Eng Mater Technol 1986;108:206–13. https://doi.org/10.1115/1.3225868.
[67] Vecchio RS, Hertzberg RW. A rationale for the "apparent anomalous" growth behavior of short fatigue cracks. Eng Fract Mech 1985;22:1049–60. https://doi.org/10.1016/0013-7944(85)90043-8.
[68] Santus C, Taylor D. Physically short crack propagation in metals during high cycle fatigue. Int J Fatigue 2009;31:1356–65. https://doi.org/10.1016/j.ijfatigue.2009.03.002.
[69] Yoshinaka F, Nakamura T, Takeuchi A, Uesugi M, Uesugi K. Initiation and growth behaviour of small internal fatigue cracks in Ti-6Al-4V via synchrotron radiation microcomputed tomography. Fatigue Fract Eng Mater Struct 2019;42:2093–105. https://doi.org/10.1111/ffe.13085.
[70] Messager A, Junet A, Palin-Luc T, Buffiere J-Y, Saintier N, Ranc N, et al. In situ synchrotron ultrasonic fatigue testing device for 3D characterisation of internal crack initiation and growth. Fatigue Fract Eng Mater Struct 2020;43(3):558–67.
[71] Taylor D. On the use of P-a plots to model the behaviour of short fatigue cracks. Int J Fatigue 1992;14:163–8. https://doi.org/10.1016/0142-1123(92)90369-N.
[72] Murakami Y, Endo M. Effects of defects, inclusions and inhomogeneities on fatigue strength. Int J Fatigue 1994;16:163–82. https://doi.org/10.1016/0142-1123(94)90001-9.
[73] Kitagawa H, Takahashi S. Applicability of fracture mechanics to very small cracks or the cracks in the early stage. Proc. of 2nd Int. conf. Mech Behaviour of Materials, American Society of Metals 1976:627–31.
[74] El Haddad MH, Smith KN, Topper TH. Fatigue crack propagation of shorts cracks. J Eng Mater Technol 1979;101:42–6.
[75] Murakami Y, Kodama S, Konuma S. Quantitative evaluation of effects of non-metallic inclusions on fatigue strength of high strength steels. I: Basic fatigue mechanism and evaluation of correlation between the fatigue fracture stress and the size and location of non-metallic inclusions. Int J Fatigue 1989;11:291–8. https://doi.org/10.1016/0142-1123(89)90054-6.
[76] Murakami Y, Usuki H. Quantitative evaluation of effects of non-metallic inclusions on fatigue strength of high strength steels. II: Fatigue limit evaluation based on statistics for extreme values of inclusion size. Int J Fatigue 1989;11:299–307. https://doi.org/10.1016/0142-1123(89)90055-8.
[77] Persenot T, Burr A, Dendievel R, Buffière J-Y, Maire E, Lachambre J, et al. Fatigue performances of chemically etched thin struts built by selective electron beam melting: Experiments and predictions. Materialia 2020;9:100589.
[78] ASM International, Lampman SR, ASM International, editors. Fatigue and fracture. [10. ed.], 3. print. Materials Park, Ohio: ASM International; 2002.
[79] Newman Jr JC, Ruschau JJ. The stress-level effect on fatigue-crack growth under constant-amplitude loading. Int J Fatigue 2007;29:1608–15. https://doi.org/10.1016/j.ijfatigue.2006.11.003.
[80] Frost NE, Dugdale DS. The propagation of fatigue cracks in sheet specimens. J Mech Phys Solids 1958;6:92–110. https://doi.org/10.1016/0022-5096(58)90018-8.
[81] Frost NE, Pook LP, Denton K. A fracture mechanics analysis of fatigue crack growth data for various materials. Eng Fract Mech 1971;3:109–26. https://doi.org/10.1016/0013-7944(71)90003-8.
[82] Huynh J, Molent L, Barter S. Experimentally derived crack growth models for different stress concentration factors. Int J Fatigue 2008;30:1766–86. https://doi.org/10.1016/j.ijfatigue.2008.02.008.
[83] Molent L, Jones R. A stress versus crack growth rate investigation (aka stress – cubed rule). Int J Fatigue 2016;87:435–43. https://doi.org/10.1016/j.ijfatigue.2016.02.029.
[84] Jones R, Molent L, Pitt S. Similitude and the Paris crack growth law. Int J Fatigue 2008;30:1873–80. https://doi.org/10.1016/j.ijfatigue.2008.01.016.
[85] Sigler D, Montpetit MC, Haworth WL. Metallography of fatigue crack initiation in an overaged high-strength aluminum alloy. MTA 1983;14:931–8. https://doi.org/10.1007/BF02644299.
[86] Bozek JE, Hochhalter JD, Veilleux MG, Liu M, Heber G, Sintay SD, et al. A geometric approach to modeling microstructurally small fatigue crack formation: I. Probabilistic simulation of constituent particle cracking in AA 7075-T651. Modelling Simul Mater Sci Eng 2008;16(6):065007.
[87] Hochhalter JD, Littlewood DJ, Christ RJ, Veilleux MG, Bozek JE, Ingraffea AR, et al. A geometric approach to modeling microstructurally small fatigue crack formation: II. Physically based modeling of microstructure-dependent slip localization and actuation of the crack nucleation mechanism in AA 7075-T651. Modelling Simul Mater Sci Eng 2010;18(4):045004.
[88] Payne J, Welsh G, Christ Jr RJ, Nardiello J, Papazian JM. Observations of fatigue crack initiation in 7075–T651. Int J Fatigue 2010;32:247–55. https://doi.org/10.1016/j.ijfatigue.2009.06.003.
[89] Jin Y, Cai P, Wen W, Nagaumi H, Xu B, Zhang Y, et al. The anisotropy of fatigue crack nucleation in an AA7075 T651 Al alloy plate. Mater Sci Eng, A 2015;622:7–15.
[90] Barter SA, Sharp PK, Holden G, Clark G. Initiation and early growth of fatigue cracks in an aerospace aluminium alloy. Fatigue Fract Eng Mater Struct 2002;25:111–25. https://doi.org/10.1046/j.1460-2695.2002.00482.x.
[91] Barter SA, Molent L, Wanhill RJH. Typical fatigue-initiating discontinuities in metallic aircraft structures. Int J Fatigue 2012;41:11–22. https://doi.org/10.1016/j.ijfatigue.2011.10.017.
[92] van der Walde K, Hillberry BM. Initiation and shape development of corrosion-nucleated fatigue cracking. Int J Fatigue 2007;29:1269–81. https://doi.org/10.1016/j.ijfatigue.2006.10.010.
[93] Molent L, Barter SA, Wanhill RJH. The lead crack fatigue lifing framework. Int J Fatigue 2011;33:323–31. https://doi.org/10.1016/j.ijfatigue.2010.09.009.
[94] Forman RG. Study of fatigue crack initiation from flaws using fracture mechanics theory. Eng Fract Mech 1972;4:333–45. https://doi.org/10.1016/0013-7944(72)90048-3.
[95] El Haddad MH, Topper TH, Topper TN. Fatigue life predictions of smooth and notched specimens based on fracture mechanics. J Eng Mater Technol 1981;103:91–6. https://doi.org/10.1115/1.3224996.
[96] Newman Jr JC, Swain MH, Phillips EP. An assessment of the small-crack effect for 2024–T3. Small Fatigue Cracks 1986:427–52.
[97] Newman Jr JC. The merging of fatigue and fracture mechanics concepts: a historical perspective. Prog Aerosp Sci 1998;34:347–90. https://doi.org/10.1016/S0376-0421(98)00006-2.
[98] Newman Jr JC, Anagnostou EL, Rusk D. Fatigue and crack-growth analyses on 7075–T651 aluminum alloy coupons under constant- and variable-amplitude loading. Int J Fatigue 2014;62:133–43. https://doi.org/10.1016/j.ijfatigue.2013.04.020.
[99] Goto M, Nisitani H. Inference of a small-crack growth law based on the S-N curve. Trans Japanese Soc Mech Eng 1990;A56:1938–44.
[100] Tanaka K, Akiniwa Y. Fatigue crack propagation behaviour derived from S-N data in very high cycle regime. Fat Frac Eng Mat Struct 2002;25:775–84. https://doi.org/10.1046/j.1460-2695.2002.00547.x.